Al–20Sn–1Cu self-lubricating alloy: Correlations between microstructure coarsening, mechanical, and application properties

Sarah de Albuquerque, Vinicius Leme Andrade, Rodrigo V Reyes, Guillaume Reinhart, Danielle Cristina Camilo Magalhães, Henri Nguyen-Thi, José Eduardo Spinelli

Al–20Sn–1Cu self-lubricating alloy: correlations between microstructure coarsening, mechanical, and application properties

Sarah De Albuquerque [1,2], Vinicius Leme Andrade [3], Rodrigo V. Reyes[2], Guillaume Reinhart [1], Danielle Cristina Camilo Magalhães [2,3], Henri Nguyen-Thi [1] and José Eduardo Spinelli [2,3,*]

1 Aix Marseille Univ, Université de Toulon, CNRS, IM2NP, Marseille, France
2 Federal University of São Carlos, Graduate Program in Materials Science and Engineering, 13565-905 São Carlos, SP, Brazil
3 Department of Materials Engineering, Federal University of São Carlos, 13565-905 São Carlos, SP, Brazil

Submitted to:

Journal of Materials Research and Technology

March 2025

Abstract

This study investigated the microstructure, microhardness, tensile strength, and dry wear behavior of the cast Al-20Sn-1Cu alloy (wt. %), focusing on the relationship between β-Sn phase morphology and the results. The Al-Sn-Cu alloys have been shown to be promising for plain bearing applications due to their self-lubricating properties. However, those alloys exhibit peculiar behaviors contrary to the classical Archard equation, which relates hardness to wear resistance, or to the typical behavior of metallic alloys, where increasing strength generally leads to a reduction in ductility. This can be attributed to the morphology, fraction and distribution of the β-Sn phase, a component of low hardness and strength but essential for self-lubricating functionality. In this study, the Al-20Sn-1Cu alloy solidified under a wide range of cooling rates varying from 1.0 to 28.9 °C/s was investigated. Dendritic spacing was measured using an automated method proposed in this study. The results showed that more refined samples had better tensile properties but compromised wear behavior. When the microstructure was refined up to dendritic spacing of 15.7 μm, a good combination between strength and ductility was achieved: a tensile strength of 72 MPa and an elongation of 14% were obtained. These results can be explained by the increased contact area between the α-Al and β-Sn phases, which favors a strain hardening mechanism. However, these samples have very small β-Sn particles, which are insufficient to form an effective lubricating layer, resulting in severe wear due to adhesion. Despite that, it achieved a lower wear coefficient compared to other self-lubricating alloys reported in the literature.

Keywords: Al-alloys, self-lubricating alloys, solidification, microstructure, wear, mechanical properties.

* E-mail address: spinelli@ufscar.br

1. Introduction

Self-lubricating alloys are commonly used in advanced plain bearings – components designed to support radial loads and ensure smooth torque transmission from a rotating shaft. These bearings usually have a cylindrical structure composed of a housing and a thin inner layer made of this tribologically material, which remains in direct contact with the shaft during operation [1–4]. In their traditional form, self-lubricating alloys consist of a hard matrix embedded with soft particles, which form a lubricating film at the interface during solid-solid contact, thereby reducing friction and wear [5,6]. For effective performance, these soft particles must be tribologically compatible with the shaft surface, as this prevents material adhesion during sliding [6]. Beyond tribological compatibility, however, sliding bearing materials must possess a combination of properties to meet specific requirements. For instance, sufficient bearing load capacity is required, yet its hardness must be as low as possible to prevent damage to the shaft and to absorb foreign particles. Corrosion and fatigue resistance are also essential characteristics [1,6]. Aluminum alloys, in particular, offer high fatigue strength, lightness, ease of forming and machinability properties, excellent corrosion resistance, high thermal conductivity and low cost, making them good candidates for bearing material matrices [1,7–10].

Regarding the lubricating element in aluminum alloys, the literature identifies some low-solubility elements including, bismuth [3,11–13], indium [14] and lead [3] to form the second phases and perform as lubricants. Lead, in particular, exhibits favorable tribological properties with steels shafts and forms the basis of the renowned sliding bearing alloy, known as Babbitt alloys [1]. However, due to Pb toxicity, these alloys are no longer viable, and Al-Sn based alloys are emerging as promising alternatives. Several studies have been performed on these alloys, particularly focusing on those with high Sn content alloyed with hardening elements such as Si and Cu [2,4,15,16] as well as on alternative manufacturing techniques to traditional metallurgical process. Notably those involving powder metallurgy [17–19] and stirring during solidification [15,20], which aim to produce extremely refined microstructures or dual structures [21].

A particularity in self-lubricating alloys merits attention with respect to the other alloys studied in terms of wear behavior. The conventional wear behavior is delineated in accordance with Archard's wear law, wherein volume loss values are directly proportional to the sliding distance and inversely proportional to the hardness value. A significant body of research has been dedicated to investigating the correlation between increasing hardness and the enhancement of tribological behavior in aluminum alloys. For instance, studies have examined the incorporation of hard ceramic particles [8–10], the addition of hard reinforcing phases such as Si [22], MgZn [23], Ni [24], and even heat treatment [7] finding that enhanced wear resistance is observed as hardness increases. Conversely, self-lubricating alloys have been shown to resist wear through the grinding and/or melting of their soft particles, thereby forming a lubricating and protective layer. The relationship between hardness and wear resistance can be inverse or more complex, with the distribution and size of the lubricating particles playing a crucial role.

Research on Al cast alloys with a soft second phase, including the Al-(15-20)%Sn alloy studied by Cruz et al. [22], the ternary high Cu content Al-20%Sn-10%Cu alloy studied by Bertelli et al. [16], the ternary Al-20%Sn-5%Zn alloy studied by Barros et al. [25], and the Al-5%In alloy studied by Freitas et al. [14], substantiate this assertion as proved a correlation between enhanced wear resistance and the presence of coarser microstructures, which in turn are associated with lower hardness and mechanical strength. Conversely, Al alloys with elevated Sn content and composed of nanostructured phases, produced by powder metallurgy or involving stirring during solidification demonstrate enhanced tensile properties and wear behavior in refined microstructures [15,17–19]. These findings highlight the need to improve understanding and find a compromise between strength and wear resistance in self-lubricating alloys with a high Sn content, which can be achieved by carefully controlling the microstructure, especially in cast alloys, since casting is a common process for self-lubricating bearings.

Furthermore, the existence of hard phases has the potential to compromise the safety of shafts and bearings. In the absence of effective control over reinforcement particles, the propagation of cracks and brittle fractures can happen at low levels of reinforcement, despite the presence of a ductile matrix [10]. In cases where the matrix exhibits a lower degree of hardness compared to the particles or if the particles are

not adequately anchored within the matrix, they can become dislodged, thereby functioning as an additional abrasive agent and exacerbating wear [23,24]. Self-lubricating alloys with soft phases are less prone to this risk and, as the name suggests, can promote self-lubrication. These alloys are particularly interesting objects of study, as they function well in the absence of lubrication and are resilient to disruptions in lubrication supply.

The present study proposes an optimized approach to evaluating the mechanical and wear behavior of the low Cu-content Al-20Sn-1Cu alloy, whose composition is close to that of the commercial bearing alloy SAE 783 [1], distinguishing it from previous investigations that primarily examined alloys with higher Cu levels undergoing a monotectic reaction [12,19]. The influence of the β-Sn phase on wear behavior is deeply analyzed, highlighting the critical role of its morphology, distribution, and adhesion in determining performance beyond conventional hardness-based models typically applied to as-cast alloys. An advanced and more efficient method for measuring dendritic spacing will be introduced, enhancing the accuracy and reproducibility of the microstructural quantification. The various computational methods and characterization techniques used can provide new insights into controlling the microstructure and properties of the alloy. In addition, the influence of the microstructure coarsening on the wear and strength will also be highlighted.

2. Experimental procedure

2.1. Thermodynamic calculation - CALPHAD method

From this point forward, the alloy under consideration will be designated as Al-20Sn-1Cu, with all compositions expressed in weight percentage, unless otherwise indicated. To fully understand the microstructure and properties of an alloy, it is relevant to determine the successive transformations occurring during solidification. To achieve this, the solidification path of the alloy under investigation was calculated from the equilibrium phase diagram using the CALPHAD method, with the support of the Thermo-Calc software and the TCAL 7.1 database.

2.2. Directional solidification process and thermal variables acquisition

The Al-20Sn-1Cu alloy was prepared by melting commercially pure elements in the stoichiometric weight ratio in an induction furnace (Inductotherm VIP Power-Trak induction furnace, Rancocas, NJ, USA). The compositions of the elements used to prepare these alloys are shown in Table 1. The alloy was solidified in a specially designed apparatus for upward directional solidification, as detailed previously [28]. This apparatus enables the production of a wide range of solidification microstructures within a single casting experiment. Heat extraction occurs exclusively through a water-cooling system at the base of the ingot. A growing thermal barrier is formed as the solidified volume increases, making the heat flow transient. This phenomenon leads to a reduction in both the thermal gradient and growth rate along the height of the ingot.

To record the temperature (T) variations over time (t), eight K-type thermocouples were positioned along the height of the ingot, as informed in Figure 1. Data was collected at a frequency of 5 Hz.

Table 1 – Chemical composition (wt.%) of metals used to prepare the alloy.

Element	Al	As	Bi	Cd	Cu	Fe	Pb	Sb	Si	Sn	Zn
Al	99.85	-	-	-	-	0.09	-	-	0.05	-	0.01
Sn	-	0.001	0.002	0.002	0.003	0.002	0.004	0.002	-	99.979	0.001
Cu	-	-	-	-	99.9	-	-	-	-	-	-

The cooling rate at each thermocouple position (P) was determined through the time derivative of the cooling curves, at the time the liquidus front passed by each thermocouple, $R(t_L) = dT/dt$. The specific methodology is described in previous work [29]. Figure 1 provides a descriptive illustration of the unidirectionally solidified ingot and the positions of the specimens along the ingot length. Figure 1a) illustrates a general relationship between the distance from the water-cooled surface, cooling rate, and microstructure coarsening. It shows that the cooling rate decreases with increasing distance from the bottom and explains that the dendritic length-scale is expected to increase accordingly, regardless of the grain morphology. Figure 1b) indicates the locations of the metallographic and microhardness specimens, which are taken from the surface perpendicular to the solidification direction, at the same positions as the

thermocouples (6 mm, 10 mm, 15 mm, 20 mm, 25 mm, 45 mm, 70 mm, and 90 mm). Figures 1c) and 1d) show the positions chosen for the wear and tensile specimens, respectively. The wear test specimens have been taken from the first and last thermocouple positions (6 and 90 mm).

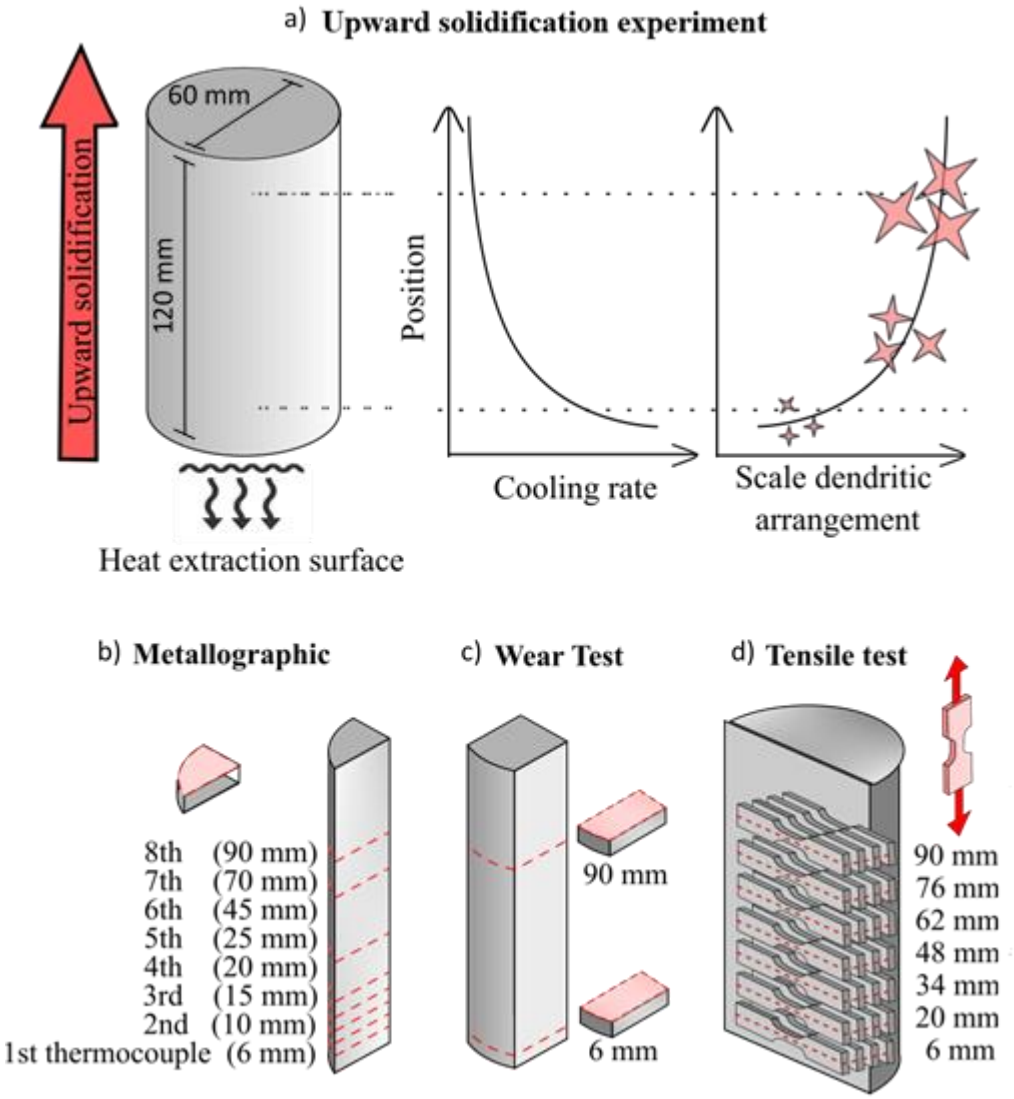

Figure 1 – a) Schematic representation of the upward solidification, cooling rate and microstructure length-scale according to position in the ingot with scale; b) the relative positions of the samples extracted for metallography and microhardness analysis, and schemes for c) wear and d) tensile tests.

2.3. Microstructural morphology evaluation and chemical analysis

For the investigation of macrosegregation along the length of the ingot, an Inductively Coupled Plasma Optical Emission Spectroscopy – ICP-OES chemical analysis was performed on two samples of about 10 grams each, taken from the positions of the bottom and the top of the ingot. The phase identification on the samples obtained from analogous locations was performed by X-ray diffraction (XRD) (Bruker D8 Advance ECO, Massachusetts, USA) utilizing Cu-Kα radiation (λ = 1.5406 Å). Diffraction patterns were acquired in the 2θ range of 10-90° with a step size of 0.02°. Phase identification was performed by comparing the observed diffraction peaks with those of known phases (α-Al [30], β-Sn [31], and θ-Al_2Cu [32].

The macrostructure of the ingot was observed on the central longitudinal surface after polishing and etching by swabbing using the Poulton's solution (12 mL HCl + 6 mL HNO_3 + 1 mL HF + 1 mL H_2O). To examine the microstructure along the cooling direction, eight cross-sectional samples were extracted from specific thermocouple positions in the ingot (Figure 1). These samples were polished and etched by immersion for 10 seconds into the Keller's etchant (2 mL HF, 3 mL HCl, 5 mL HNO_3, and 75 mL H_2O) to reveal the dendritic structure. The samples were then analyzed using optical microscopy (OM) to measure dendritic spacing, using an Olympus BX41M-LED (Tokyo, Japan) microscope. Additionally, scanning electron microscopy (SEM) equipped with an energy dispersive spectroscopy (EDS) detector in a Philips XL-30 FEG microscopy was used for chemical identification, morphology analysis, and examining worn surfaces. Image quantification was performed using ImageJ software [33,34].

The triangle method for measuring primary dendrite arm spacing (λ_1) [35] was not feasible due to the irregular dendritic microstructure. As a result, the authors developed and applied a technique adapted from the Heyn linear intercept method [36]. In this approach, the dendritic arm spacing (DAS) was calculated by determining the ratio of dendritic arms intersected by a line of known length. The process was automated using ImageJ software, where the micrographs were segmented into two regions—dendritic and interdendritic—using machine learning based on color and shape differences [37]. A macro script was then implemented in ImageJ to draw 100 lines of known length at varying angles from corner to corner of

the image, count the number of intersections with the dendritic region, and normalize by the line length. Further methodological details are provided in *Appendix A*.

The X-ray computed tomography (XCT) technique was applied to study the morphology of the β-Sn phase, providing a 3D reconstruction of the samples and therefore more detail on the microstructure compared to a 2D micrograph. These analyses were carried out on samples taken from the positions of the lowest cooling rate at the top of the ingot (1.0 °C/s), an intermediate cooling rate (5.5 °C/s) and the highest cooling rate at the bottom of the ingot (28.9 °C/s). The images were taken with a Synchrotron light source at a high-brightness of 22 keV (Mahogany line at SIRIUS-CNPEM, Campinas-Brazil). For each 3D image, the reconstruction was carried out using an algorithmic projection filter, processing 2048 projections. The voxel size was 546 nm. Considering 5 voxels are required to reliably define the morphology, the resolution of the analysis was estimated to be approximately 2.5 μm. The result was analyzed using the Avizo (2022.1) software (Thermo Fisher Scientific, Waltham-USA).

After obtaining the 3D tomography data, non-local means and unsharp masking filters were applied to reduce noise and enhance contrast. The variation in gray intensity caused by the difference in X-ray absorption of the Al and Sn was used to segment the interdendritic β-Sn phase using a grayscale threshold. The individually segmented β-Sn phase was filtered to sharp the boundaries between phases and exclude small spots of artifacts from the radiographs. The segmentation results allowed for measurements of volume fraction, surface area and average trunk radius of the interdendritic phase.

2.4. Tensile tests and hardness measurements

To analyze the effects of microstructural features on mechanical properties, rectangular dog-bone shaped tensile specimens with a length of 30 mm, width of 4 mm and thickness of 2 mm were machined from the ingot. The tensile specimens were taken in quadruplicate and transverse to the direction of solidification growth, as shown in Figure 1. The central positions of the specimens correspond to 6 mm, 20 mm, 34 mm, 48 mm, 62 mm, 76 mm, and 90 mm from the water-cooled bottom, and therefore the results of the tensile tests were related to the microstructures and cooling rate with respect to these positions. The

dimensions of these specimens were proportional to those standardized by ASTM E8/E8M 21 [38], and the tensile results were considered compatible with the results of the specimens on a standardized scale, as has been done in another work [28]. The graphs and tensile properties were conceived with the average values of the quadruplicate tests, with the error bars representing the range of the maximum and minimum measurements.

The tensile tests were performed at a strain rate of 3.0×10^{-3} s^{-1} using a Universal Instron 5500R machine (Instron, Massachusetts, EUA) with a 250 KN load cell. The results and discussions are based on the true stress and strain values calculated from the strain and force values provided in the tensile test, with the exception of toughness, which was calculated using the engineering stress-strain curve, based on the following empirical approximation, described in Equation 1:

$$\sigma_T = \frac{\sigma_Y + \sigma_{UTS}}{2} \times \varepsilon_U \quad [1]$$

Where σ_Y is the yield tensile strength, σ_U is the ultimate tensile strength, and ε_U uniform elongation at fracture experimentally measured. Considering that strain localization is the critical event during the wear of ductile tribological alloys, Bravo *et al.* [6] suggested that the yield strength and the strain hardening exponent (*n*) are the main quantitative parameters for the evaluation of sliding bearing alloys. Thus, the strain hardening exponent (*n*) was calculated from the Hollomon equation [39] according to Equation 2:

$$\sigma = Q\varepsilon^n, \quad [2]$$

where σ and ε are the true stress and strain, Q is the strength coefficient and n is the strain-hardening exponent.

Vickers microhardness tests were performed on transverse sections of the metallography samples using a Shimadzu model HMV-G20ST (Kyoto, Japan) durometer. The average hardness measured was obtained from at least twenty indentation tests (indentation load of 0.5 kg and dwell time of 10 s).

2.5. Wear tests

The wear test samples were extracted perpendicularly along the length of the ingot, as shown in Figure 1, with the aim of allowing a single DAS to be associated with each sample. The tests were carried out using a micro-adhesive wear machine (ball crater), where a rotating steel ball (AISI 52100, 25.4 mm diameter, 818 HV) was rolled against the sample, forming a wear crater, as detailed in the Refs. [12,40]. The ball sliding speed was 260 rpm, and a normal contact load of 0.6 N was applied, following [22]. These tests were performed on samples taken from the positions of the bottom and the top of the ingot to encompass a wider range of solidification conditions.

The tests produced cap-shaped impressions on the sample surfaces. The wear volumes (V_W) were calculated using Equation 3, based on the arithmetic mean of four diameter measurements taken from each cap, where *d* is the average cap diameter and *R* is the sphere radius [12]. The tests lasted between 20 and 200 minutes, with measurements taken at 20-minute intervals. Table 2 shows the time intervals and the corresponding sliding distances. To ensure that only the microstructure influenced the results, the tests were performed without the use of any lubricants or abrasive particles.

Table 2 - The time intervals and the corresponding sliding distances of the wear tests.

Time (min)	20	40	60	80	100	120	140	160	180	200
Sliding distance (m)	417	835	1252	1669	2087	2504	2922	3339	3756	4174

$$V_W = \frac{\pi . d^4}{64 . R} \quad [3]$$

A traditional manner of quantifying wear behavior is through the classic Archard relationship (Equation 4), which relates the volume worn (V_W), the sliding distance (*m*), the normal load (*N*) and the hardness of the softest contact surface (*H*) through a dimensionless coefficient *K*, the wear coefficient. However, for practical uses, the quantity K/H is often more useful, giving rise to a dimensional wear coefficient *k*, in units of mm^3/N.m, which represents the volume of material removed by wear per unit of sliding distance per unit of normal load on the contact. *k* was calculated in this work using Equation 5 [41]:

$$V_W = \frac{K.N.m}{H} \quad [4]$$

$$k = \frac{V_W}{m.N} \quad [5]$$

3. Results

3.1. Equilibrium solidification path

As shown in Figure 2, the equilibrium solidification path of the Al-20Sn-1Cu alloy begins with the formation of solid α-Al at 630 °C, marked by a simultaneous decrease of the liquid phase mass fraction (blue solid-line) and an increase of the solid aluminium phase (red dashed-line), continuing until 382.5 °C. Below 382.5 °C and down to the eutectic temperature (229.5 °C), the liquid phase reacts with the solid α-Al to form θ-Al_2Cu intermetallic (green dashed-dotted line). This explains the very slight decrease of both α-Al and liquid fractions, concomitantly with an increase in θ-Al_2Cu phase fraction. Finally, the remaining solute-enriched liquid solidifies via a eutectic reaction, forming the α–Al/β-Sn/Al_2Cu solid. The long temperature interval between the start of α-Al solidification and the eutectic reaction highlights the strong dependence of Sn dispersion on the microstructural scale of α-Al. Since the solubility of Sn in Al is extremely low, the β-Sn phase is nearly pure tin with its mass fraction corresponding to the nominal 20% Sn content of the alloy. The mass fractions of the β-Sn, θ-Al_2Cu and α-Al phases are 20%, 2% and 78% at 150 °C, respectively.

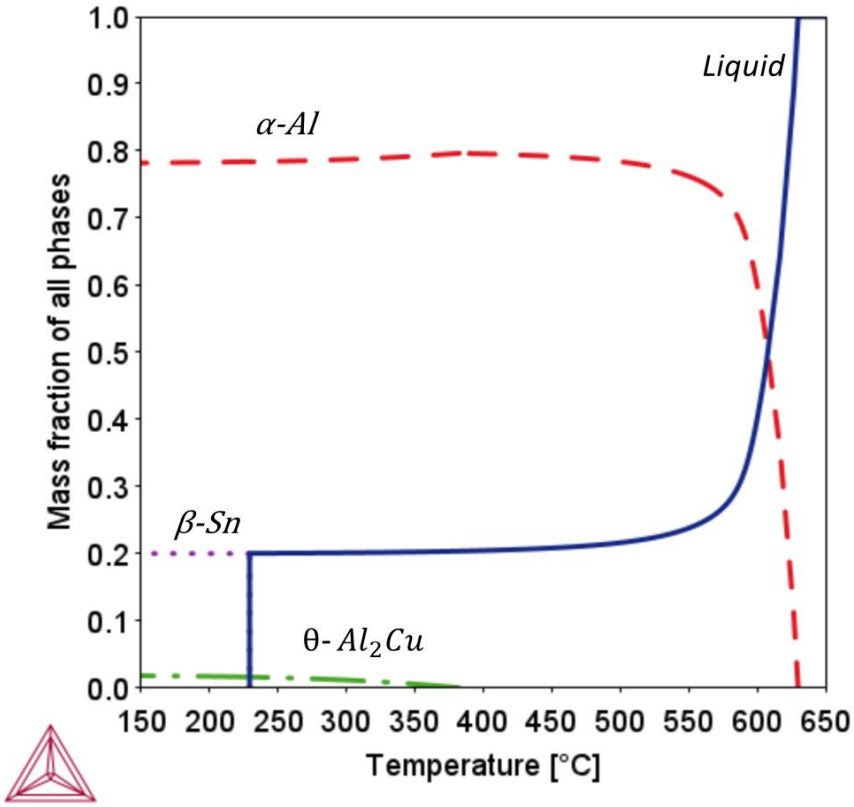

Figure 2 –Solidification path of the Al-20Sn-1Cu alloy calculated from the equilibrium phase diagram using the CALPHAD method, with the support of the Thermo-Calc software and the TCAL 7.1 database.

3.2. Solidification and morphology evolution

Figure 3 depicts the cooling curves recorded by the eight thermocouples and the macrostructure at the center surface of the ingot. Figure 3(a) shows the time delay required for the isotherms to propagate from the cooled base of the ingot, both for the experimental *liquidus* (T_L = 626.4 °C) and the eutectic temperatures (T_{eut} = 227.5 °C), confirming the unidirectional heat flow. From these curves, the cooling rates at each thermocouple position were determined, and the experimental values are presented in Table 3. Figure 3(b) shows the macrostructure along the sample, for which three zones can be identified. From the bottom to the top of the ingot, zone I, which covers the highest cooling rates, from 28.9 to 5.5 °C/s, is characterized by a high density of very small equiaxed grains. Some of these grains grew oriented to the growth direction coinciding with the heat flow. Then, a mixed zone with the coexistence of fine columnar

grains and few equiaxed grains is observed [25,42], i.e., zone II, which covers the positions cooled between 3.4 and 1°C/s. Zone III represents the blockage of columnar grains by equiaxial grains caused by a transition between growth modes, the columnar-to-equiaxial transition [43,44]. The analysis of zone III is outside the scope of this study.

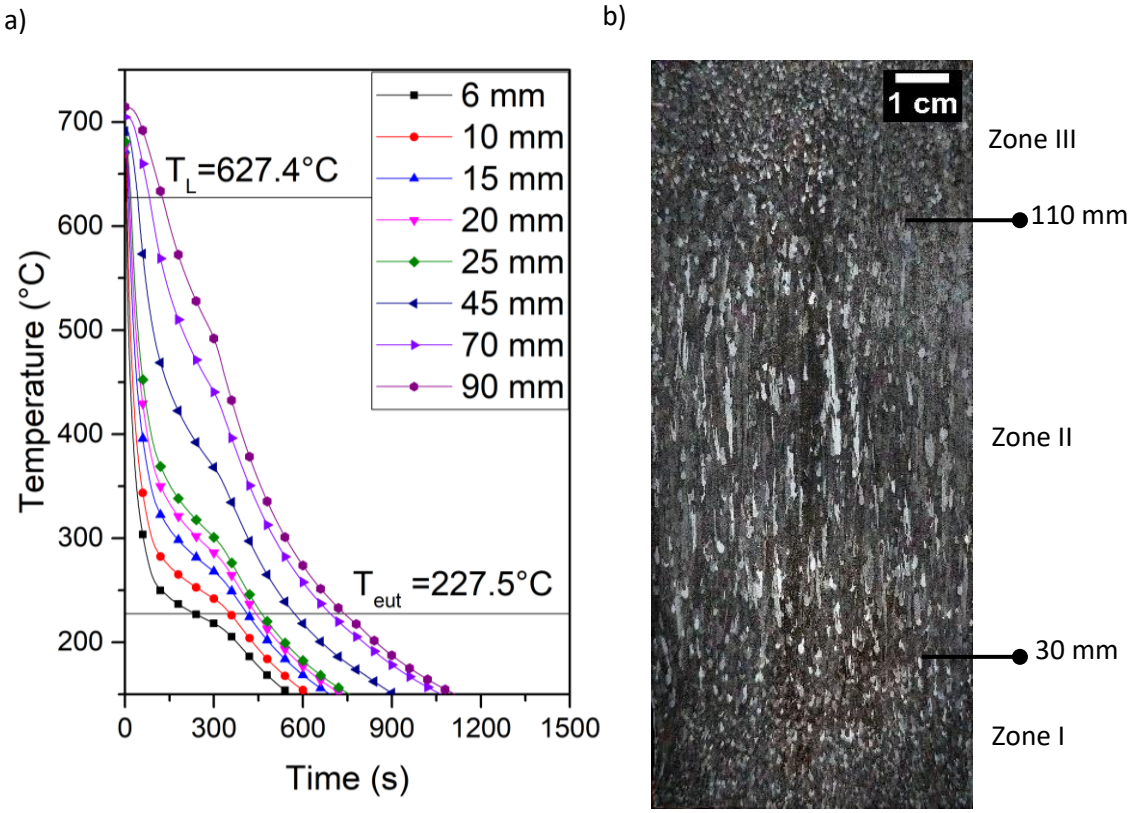

Figure 3 – (a) Cooling curves in the Al-20Sn-1Cu alloy recorded by the thermocouples highlighting the liquidus temperature and the eutectic temperature. The legend shows the positions of the thermocouples in the ingot. (b) The macrostructure at the center surface of the ingot, highlighting zone I (cooled between 28.9 and 5.5 °C/s), zone II (cooled between 3.4 and 1.0 °C/s) and zone III, located at the top of the ingot.

Table 3 – Experimental measurements of the cooling rate for each thermocouple position in the Al-20Sn-1Cu alloy.

Position – P (mm)	6	10	15	20	25	45	70	90
Cooling rate – R (°C/s)	28.9	15.2	8.3	6.4	5.5	3.4	1.7	1.0

The experimental values of the cooling rates (R) ranged from 1.0 to 28.9 °C/s and, associated with the corresponding measured DAS values, provided an experimental law, $\lambda_A = 47.70 \times R^{-0.33}$, which is plotted in Figure 4. The DAS exhibits a range from 15.7 to 49.5 μm, with the lowest value occurring in conjunction with the highest cooling rate. SEM images for the specimens cooled at 28.9, 5.5 and 1.0 °C/s are highlighted in Figure 4.

During solidification, α-Al grains initially nucleate and grow, while the solute content in the residual liquid phase increases rapidly. Consequently, the solute-rich interdendritic region (white region in Figure 4) exhibits a mixed circular and branching structure as a filling between the α-Al grains (black region in Figure 4).

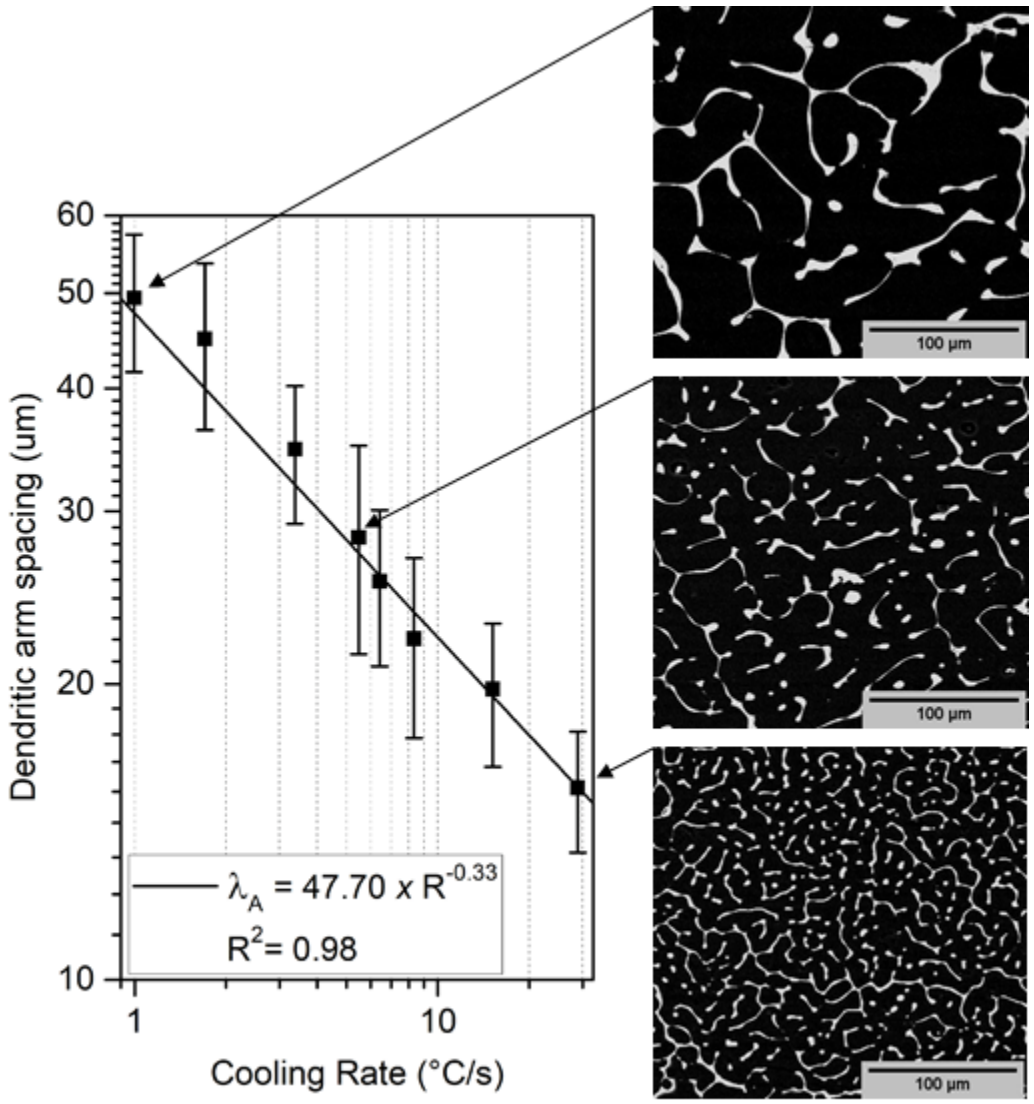

Figure 4 – Average α-Al dendritic arm spacing as a function of the cooling rate and respective SEM images of the Al-20Sn-1Cu alloy corresponding to samples cooled at 28.9, 5.5 and 1.0 °C/s. R^2 is the coefficient of determination.

The chemical composition of the phases was verified by SEM/EDS. Figure 5 depicts a representative SEM micrograph and its respective chemical mapping. The elements subjected to analysis were Al, Cu, Sn and Fe. The latter was measured as impurity in the commercially pure Al used for the alloy production. The chemical mapping in Figure 5 (b) illustrates the low solubility of Sn in Al, showing a matrix rich in Al and an interdendritic region composed of Sn with a small amount of Fe. Meanwhile Cu is

homogeneously distributed, especially throughout the α-Al matrix. The wt. % compositions of the phases were also determined. Figure 5(a) shows the typical regions analyzed, namely matrix and interdendritic region, and Table 4 presents the average results for Al, Sn, Cu and Fe from the selected EDS area analysis carried out on samples solidified at 28.9, 6.4, and 1°C/s, the same samples shown in Figure 4. The results indicate that both Cu and Fe have a very low content and are practically in solid solution into the α-Al matrix. Furthermore, phases other than β-Sn and α-Al were not formed.

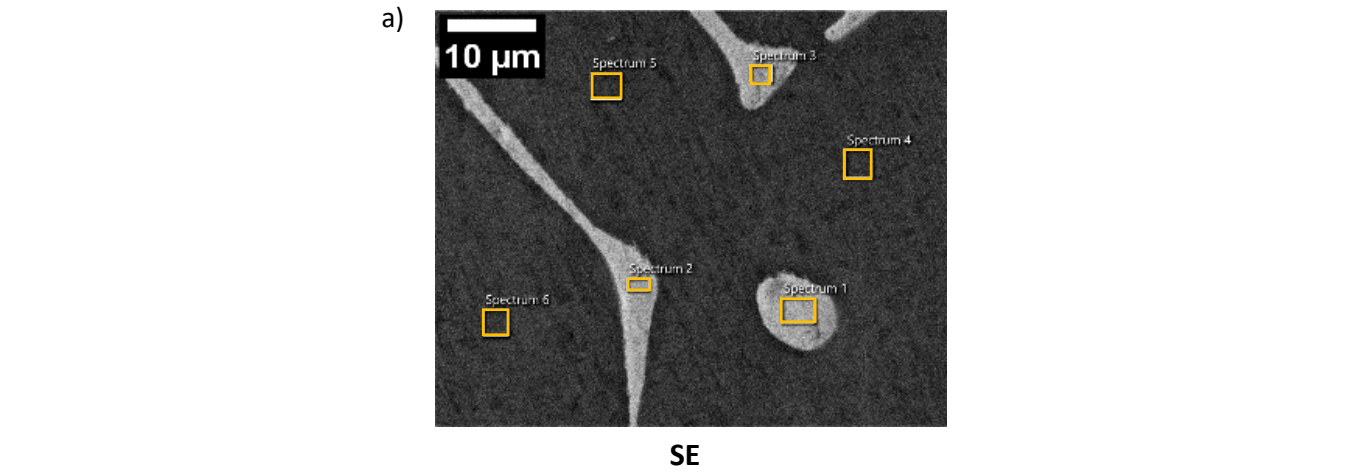

Figure 5 – (a) SEM image and (b) EDS chemical mappings of a typical sample in the Al-20Sn-1Cu alloy – cooling rate 5.5 °C/s.

Table 4 – Spot EDS chemical analysis in the interdendritic and α-Al matrix regions of the Al-20Sn-1Cu alloy (in wt.%).

Bottom of ingot – 28.9 °C/s		
Element	Matrix	Interdendritic region
Al	**99.2 ± 0.1**	4.1 ± 2.7
Fe	0.0 ± 0.0	0.1 ± 0.1
Cu	0.4 ± 0.1	0.4 ± 0.2
Sn	0.4 ± 0.2	**95.5 ± 2.7**
Middle of ingot – 5.5 °C/s		
Element	Matrix	Interdendritic region
Al	**99.5 ± 0.3**	2.5 ± 0.1
Fe	0.1 ± 0.1	0.1 ± 0.2
Cu	0.1 ± 0.1	0.7 ± 0.1
Sn	0.3 ± 0.2	**96.6 ± 0.2**
Top of ingot – 1.0 °C/s		
Element	Matrix	Interdendritic region
Al	**99.4 ± 0.1**	0.8 ± 0.1
Fe	0.0 ± 0.0	0.1 ± 0.0
Cu	0.4 ± 0.1	0.1 ± 0.2
Sn	0.1 ± 0.0	**99.0 ± 0.3**

Figure 6 shows the diffractograms for the specimens cooled at 28.9, 5.5 and 1.0 °C/s, analyzed by X-ray diffraction. The main crystalline constituents identified were, as expected: the α-Al phase (red triangle symbols), β-Sn (blue squares) and θ-Al_2Cu (green circles). In the most rapidly cooled sample (28.9°C/s), there is a predominance of the α-Al phase, with intense and defined peaks. The intensities of the β-Sn peaks converged, and the overall distribution of intensities became more uniform for this phase. In the sample cooled at an intermediate rate (5.5 °C/s) and in the slow cooled sample (1.0 °C/s), there is a progressively greater dispersion of the intensities of the α-Al phase peaks. indicating a possible morphological change in the phases, possibly related to coalescence or growth of phases and a change in the distribution of Sn. The presence of the θ-Al_2Cu phase is confirmed in all samples by the occurrence of only one characteristic peak for each spectrum, corroborating what was expected according to the thermodynamic calculations (Figure 2).

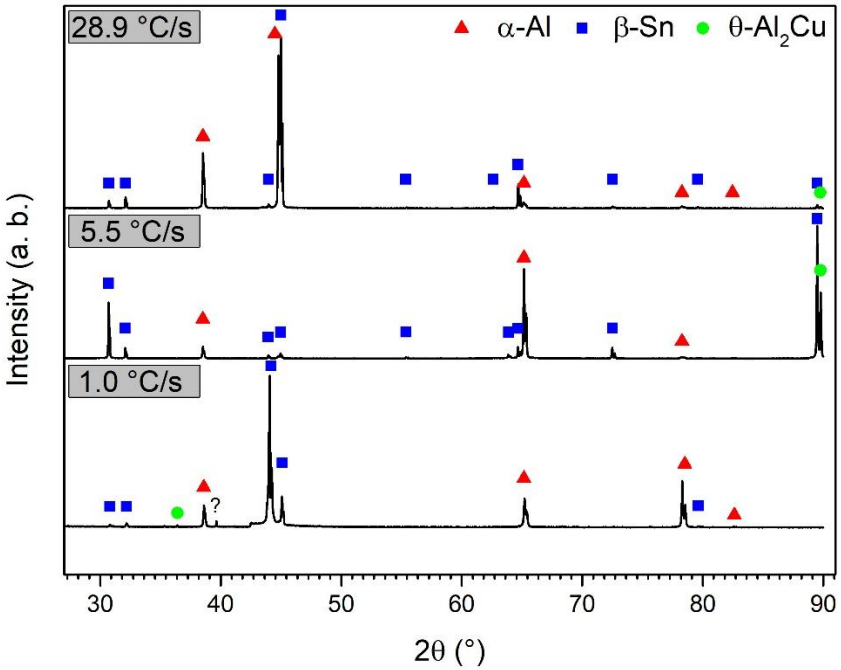

Figure 6 – X-ray diffraction (XRD) analysis performed on samples cooled at 28.9, 5.5 and 1.0 °C/s of the Al-20Sn-01Cu alloy - Triangle – α-Al, Circle – θ-Al_2Cu, and Square – β-Sn.

Figure 7 illustrates the results obtained through X-ray computed tomography (XCT) for the 1.0 °C/s, 5.5C/s and 28.9°C/s cooled samples. Segmentation and reconstruction revealed the intercontinuity of the Sn phase, throughout the interdendritic region, as a foam, which was quantified in terms of volume fraction, surface area and the average radius of the branches, the results of which are shown in Table 5.

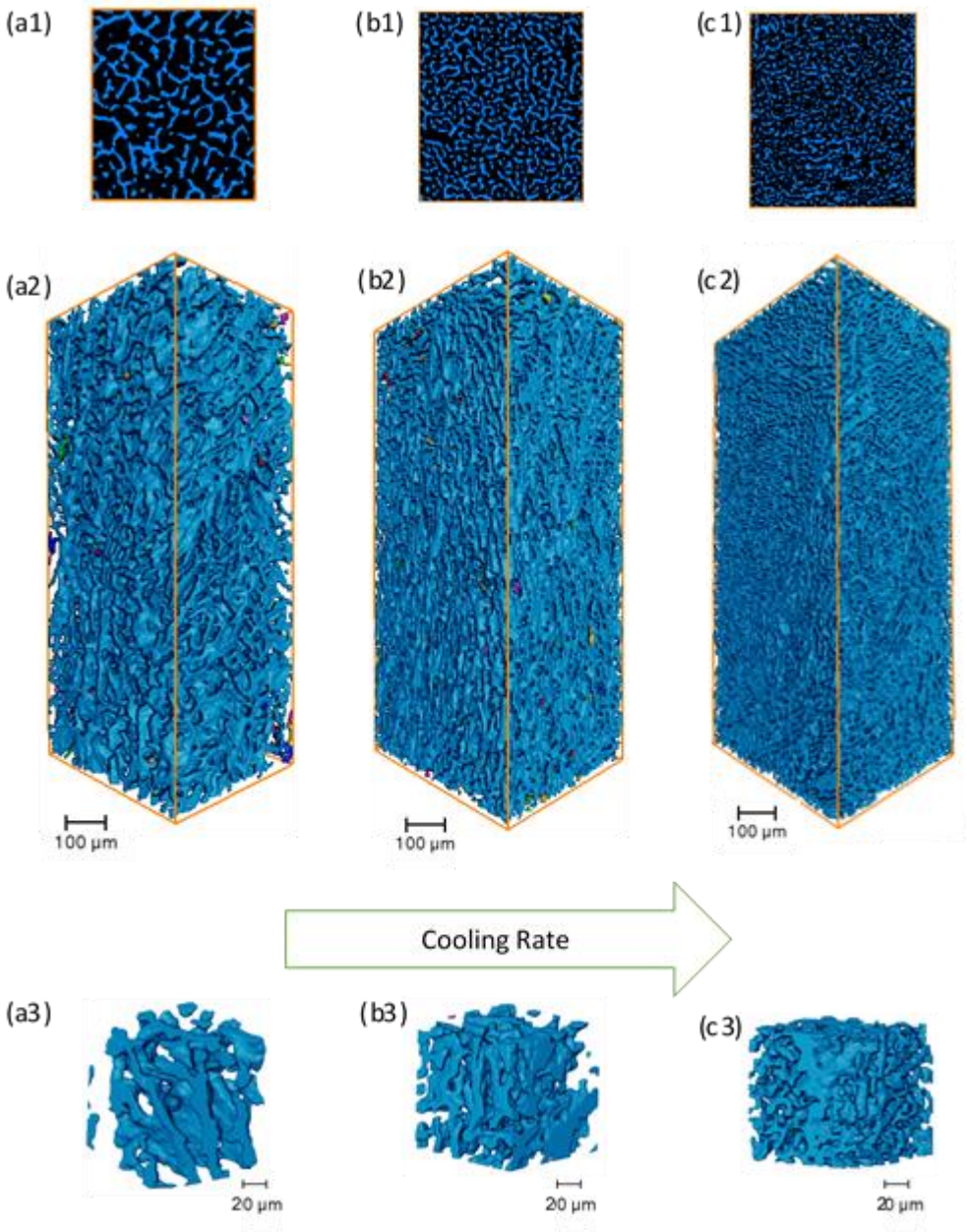

Figure 7 – Cross-sectional view from above, XCT rendering of the β-Sn phase separated at the boundaries of the α-Al dendrites, and details of the morphology in the Al-20Sn-1Cu alloy solidified at (a) 1.0°C/s, (b) 5.5°C/s and (c) 28.9°C/s after exclusion of the Al-rich phase. The arrow indicates the cooling rate increase direction.

Table 5 – Quantitative XCT results. Volume fraction, surface area and average branch radius of the β-Sn phase in the Al-20Sn-1Cu samples solidified at 1.0°C/s, 5.5°C/s and 28.9°C/s.

Sample	β-Sn Vol. fraction (%)	β-Sn Surface area (E+07 μm^2)	β-Sn Mean radius (μm)
1.0 °C/s	24.81	1.58	3.87
5.5 °C/s	27.74	2.51	2.80
28.9° C/s	26.22	3.90	1.65

The volumetric reconstructions of the Sn phase can be seen in Figures 7(a2), (b2), and (c2), revealing a distinct network structure. Due to the extremely low miscibility of Sn in Al and the fact that Sn is the last phase to solidify—as confirmed by the thermodynamic calculations in Figure 2—this element becomes concentrated in the interdendritic regions, forming an interconnected network. Through segmentation, each particle is isolated and assigned a distinct color. In all samples, a prominent blue network is observed, indicating the continuity of the entire β-Sn phase. Although segmentation identified some smaller particles, they were excluded from the analysis for consistency and comparison purposes, as their volume and size were significantly smaller compared to the main network.

A comparison of the volume fraction across the samples highlights the accumulation of solute at the bottom of the ingot. The highest Sn volume is found near the base, coinciding with a more refined microstructure. Notably, the finer sample exhibits the most complex and densely entangled network, as evidenced by its largest surface area (3.90E+07 μm^2), which is more than twice that of the slowly cooled sample (1.58E+07 μm^2). A lower cooling rate results in a sample having a less intricate network, characterized by thicker branches.

While the 2D cross-sectional views in Figures 7(a1), (b1), and (c1) help illustrate the variation in branch size, they do not offer the comprehensive insight made possible by the 3D analysis.

3.3. Macrosegregation analysis

The concentration of Sn along the length of the ingot was determined by inductively coupled plasma-optical emission spectroscopy (ICP-OES) by analyzing one sample at the top and one at the bottom of the ingot (see Figure 1). The measurements reveal a concentration of 25% Sn at the base and 20% at the top, expressed in weight percentage (wt %). It can be inferred that the distribution of Sn along the length of the ingot is characterized by inverse macrosegregation, i.e., Sn build-up at the bottom of the ingot. This is expected and has been observed in other similar studies [45] due to the difference in density between Al and Sn, 2.7 and 7.2 g/cm^3, respectively. The concentration of Cu was also analyzed and found quite constant along the ingot with results of approximately 0.3 wt.%.

In accordance with the equilibrium phase fraction diagram (Figure 2), it was anticipated that approximately 2%, in mass fraction of the θ-Al_2Cu phase would be present, exhibiting a faceted growth into long strips surrounding primary α-Al dendrites [38]. However, although the chemical analysis by EDS (Figure 5 and Table 4) did not confirm the presence of θ-phase, the XRD analysis detected characteristic peaks of this phase in the samples indicating that there was formation, albeit in small fraction.

3.4. Mechanical behavior and fracture surface analysis

To understand the influence of the dendritic length scale on the mechanical properties, the average arm spacing was correlated with the microhardness and tensile properties along the ingot. The Vickers microhardness results are shown in Figure 8, the typical real stress-strain curves corresponding to each analyzed position are shown in Figure 9, and the association of the DAS with the mechanical properties is shown in Figure 10. Yield strength, σ_Y -0.2% proof stress, and tensile strength. σ_U. are plotted on the left axis, while elongation ε is plotted on the right. The properties are plotted as a function of the DAS, λ_A, which reflects the cooling rate. The tensile properties, in addition to the strain hardening coefficient "n" from the Hollomon equation, are summarized in Table 6. The tensile properties are based on the true stress and strain values calculated from the strain and force values provided in the tensile test, except for toughness, which was calculated using the engineering stress-strain curve.

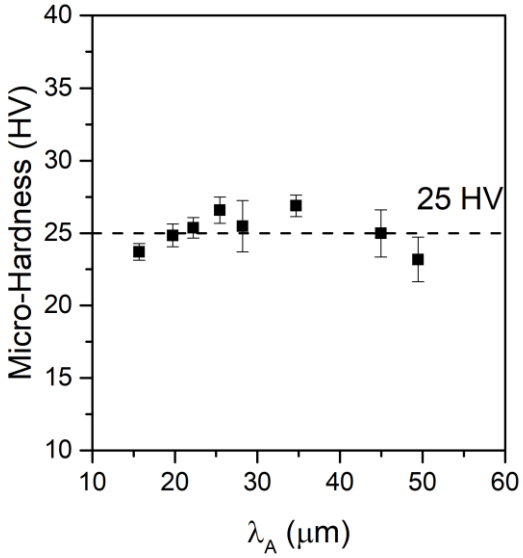

,

Figure 8 – Vickers microhardness (HV) as a function of dendritic arm spacing in the Al-20Sn-1Cu alloy.

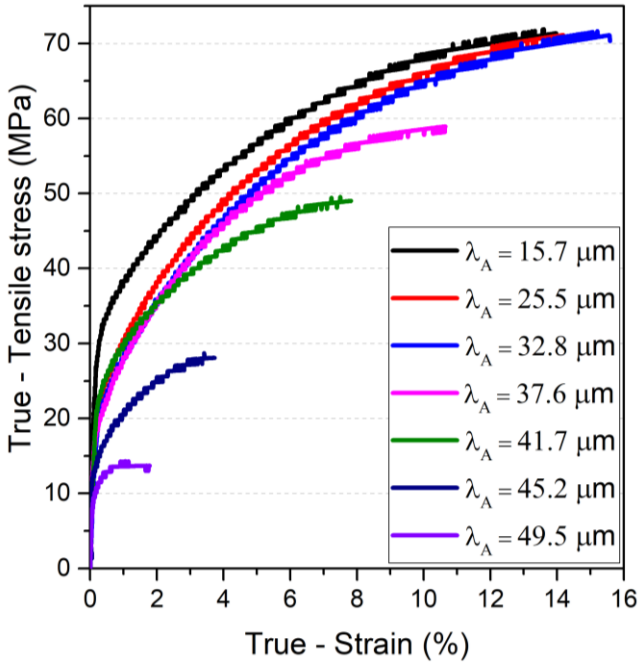

Figure 9 – True stress-strain curves representative of each of the ingot positions and their respective DAS in the Al-20Sn-1Cu alloy.

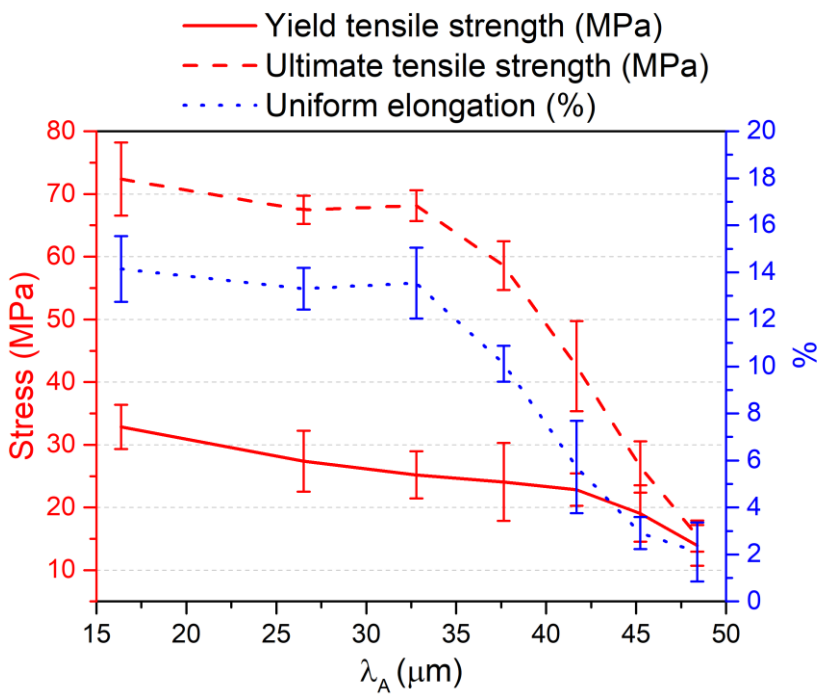

Figure 10 – Experimental correlations of the true tensile properties and DAS (λ_A) of the Al-20Sn-1Cu alloy: yield tensile strength, ultimate tensile strength and elongation-to-fracture.

Table 6 – Experimental tensile properties of the Al-20Sn-1Cu alloy. Dendritic average spacing; σ_Y: Yield tensile strength; σ_U Ultimate tensile strength; ε_u: Elongation-to-fracture; σ_T: Toughness; n: Strain hardening exponent; Q: Strength coefficient.

λ_A (μm)	σ_Y (MPa)	σ_U (MPa)	ε_U (%)	σ_T (MPa)	n	Q (MPa)
15.7	32.8	72.4	14.1	7.2	0.28	129.8
26.5	27.4	67.4	13.3	6.8	0.31	133.3
32.8	25.2	68.1	13.5	7.9	0.28	127.4
37.6	24.1	58.6	10.1	4.2	0.33	133.5
41.7	22.8	42.5	5.7	3.2	0.28	97.8
45.2	19.0	26.4	2.9	0.8	0.19	54.6
49.5	13.9	15.4	2.1	0.2	0.10	23.2

Hardness remained almost constant at around 25 HV for all specimens, regardless of microstructural coarsening or macrosegregation, as shown in Figure 8. On the other hand, the tensile properties showed a notable variation along the ingot, according to Figure 9. As the DAS decreases, the fracture is more ductile, while a brittle fracture occurs with very little deformation before rupture as the microstructure becomes coarser. This is in line with the n-exponents, which ranged from 0.28 to 0.10, and showed a marked decrease with coarser microstructures.

As can be observed in Figure 10 and Table 6, there is a continuous increase in yield tensile strength as the microstructure becomes refined. For example, it can be noted that for λ_A = 15.7 μm, the average yield strength is 32.8 MPa. For coarser microstructures, such as λ_A = 49.5 μm, the yield strength is only 13.9 MPa. Additionally, when observing the data related to tensile strength and ductility in Figure 10, an unexpected trend is noted, as there is a simultaneous increase in strength and ductility. It is noteworthy that a change in the behavior of tensile strength and elongation-to-fracture at λ_A = 32.8 μm is observed, with a sharper drop from that point onwards.

Generally, increasing the mechanical strength of an alloy is accompanied by a reduction in ductility and toughness. However, for the Al-20Sn-1Cu alloy, considering the solidification conditions adopted in this investigation, it is observed that microstructure refinement is beneficial for both strength and ductility. For instance, in the case of the microstructure with λ_A = 15.7 μm, the finest condition studied, a tensile strength of 72 MPa and a ductility of 14% were achieved. At the opposite, in the coarsest condition, a tensile strength of 16 MPa and a significantly reduced ductility of around 2% were obtained, highlighting the detrimental effects of inadequate cooling rates and dendritic coarsening. The observed behavior in this study could be attributed to the specific characteristics of the Al-20Sn-1Cu alloy system, such as β-Sn morphology and distribution, as will be discussed later.

Fractographies of the finer (λ_A = 15.7 μm) and coarser (λ_A = 49.5 μm) specimens, after tensile tests, are shown in Figure 11(a-b) and Figure 11(c-d), respectively, in order to illustrate the most extreme conditions of mechanical behavior and microstructure. There are significant differences between the two fracture surfaces that clarify the fracture mechanism. In the more refined microstructure, there is higher adhesion between the α-Al matrix and the β-Sn phase besides more homogenization of the β-Sn regions (black points). This phenomenon was observed over almost the entire fracture surface, and a representative image is shown in Figure 11(a). Details of this fractography show small dimples in the β-Sn phase on the contour between the dendrites, Figure 11(b) (indicated by black arrows). On the other hand, Figure 11(c), referring to the coarser microstructure, shows less adhesion between Al matrix and Sn, a more dispersed distribution of the interdendritic phase and the preservation of the dendritic microstructure, characteristic

of decohesive, brittle rupture. In addition, there is embrittlement of the β-Sn phase, shown in detail in Figure 11(d) (yellow arrow).

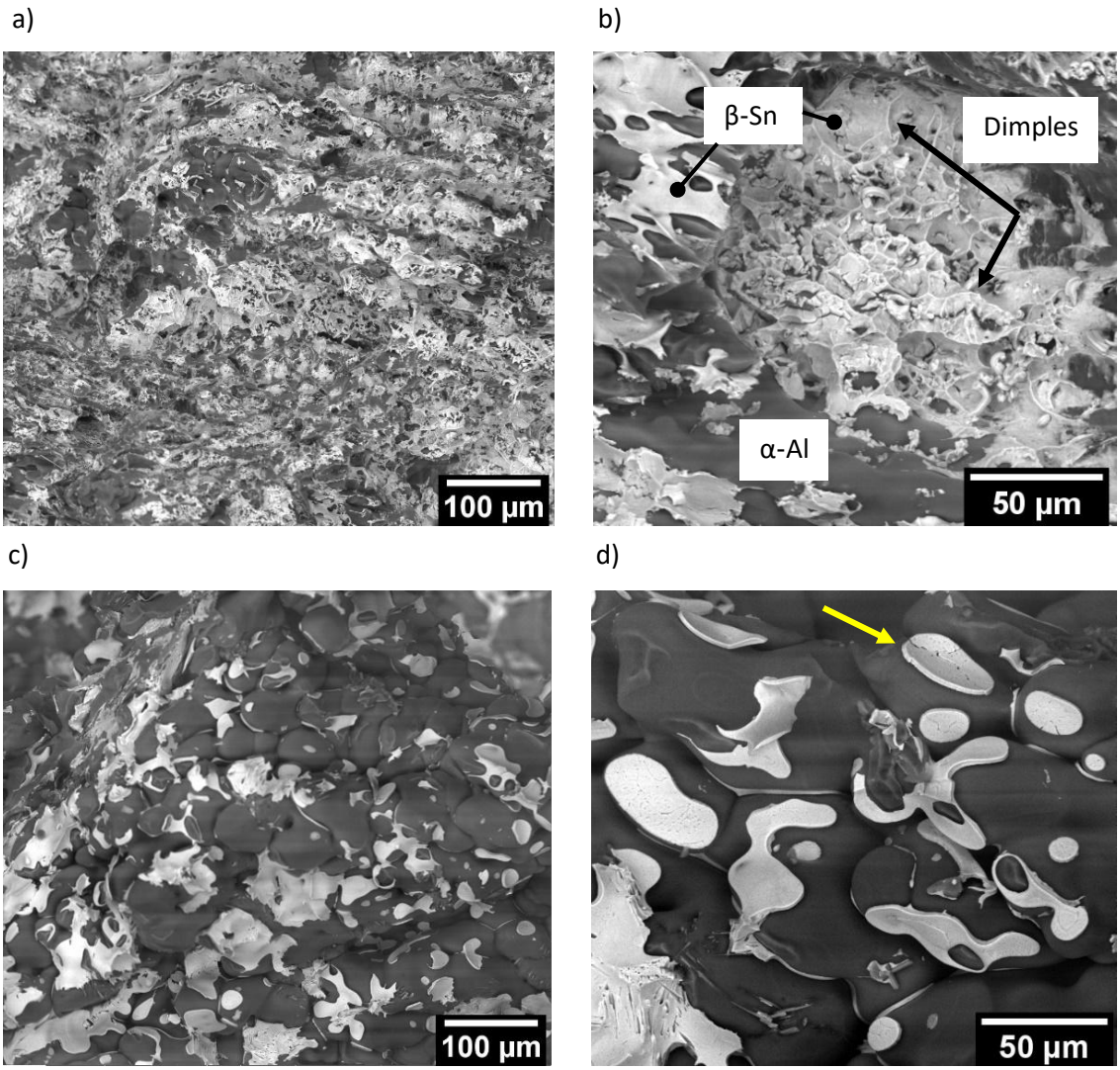

Figure 11 – Fracture surfaces of the finer sample (a-b) and the coarser samples (c-d) of the Al-20 Sn-1Cu alloy after the tensile tests. Sn in white and Al in dark gray.

3.5. Wear behavior

Quantitatively, the wear behavior was analyzed using the dimensional wear coefficient, equation [5]. Figure 12 shows the coefficient as a function of the sliding distance for samples solidified at cooling

rates of 1.0 °C/s and 28.9 °C/s, which exhibit significantly different dendritic microstructural scales and β-Sn phase morphology. A sharp increase in the volume removed was observed at the initial sliding times, followed by a stabilization of the coefficient: at 5.3×10^{-4} $mm^3/N.m$ for the most refined sample (λ_A = 15.7 μm) and at 4.5×10^{-4} $mm^3/N.m$ for the coarsest sample (λ_A = 49.5 μm). Although the experimental points are relatively close to each other, those corresponding to finer microstructures tend to have higher k values. The observation that the volume loss of the materials increases continuously with increasing sliding distance is consistent with Archard's Law and is corroborated by other studies on wear in Al alloys [7,8,10], However, the indication of a stabilization of volume loss over prolonged testing periods is of particular interest.

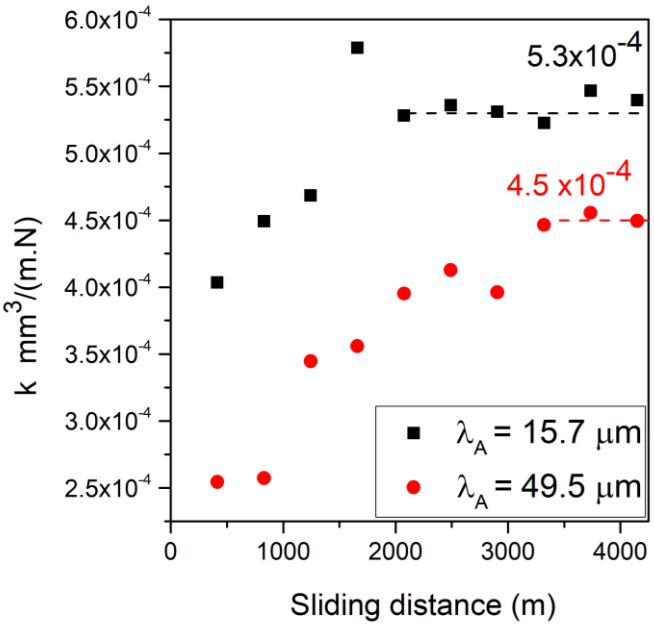

Figure 12 – Dimensional wear coefficient as a function of sliding distance evaluated on the finest (λ_A=15.7 μm) and coarsest (λ_A=49.5 μm) samples of the Al-20Sn-1Cu alloy.

Complementing the analysis of wear behavior, Figure 13 shows the worn surfaces of the two wear-tested samples, one with a finer microstructure (λA = 15.7 μm), solidified at high cooling rate (28.9°C/s) and the other with a coarser microstructure (λA = 49.5 μm) solidified at low cooling rate (1°C/s), after 4,000

m of sliding. The deformed white areas, which correspond to the β-Sn phase and are indicated as the lubricating film in Figure 13, illustrate the self-lubricating mechanism of alloys containing soft second phases [5,6,46]. The anti-friction effect arises from the extrusion of the soft phase, which forms a protective surface film that shields the friction surfaces from seizure and scoring [5]. However, the effectiveness of this film is influenced by the microstructure, as demonstrated by comparing the two samples in Figure 12 and Figures 13. It is noticeable that the lubricating film regions are smaller and more widely spaced in the more refined sample, Figure 13 (a), as well as the presence of rough surface regions, resulting from a higher proportion of material detachment (delamination). In contrast, the coarser microstructure sample exhibits larger pockets of lubricating film, more widely spaced, along with fine, shallow grooves aligned with the sliding direction, indicating a more scratched surface, as illustrated in Figure 13(b).

The results of the energy-dispersive spectroscopy (EDS) analysis of the worn surfaces of both samples are presented in Figure 14. Al, O, Sn, Fe and Cu were the elements analyzed. A significant amount of oxygen (O) can be seen in both samples, with a higher amount in the coarser sample (Figure 14b), as well as a higher amount of iron (Fe). The Sn content was also determined, yielding slightly higher values in the refined sample (Figure 14a), which is consistent with the other results presented thus far, though each sample exhibited distinct morphologies. In the refined sample, Sn appears to be more rigid with well-defined particles, while in the coarse sample, Sn appears crumpled. The SE SEM image related to the chemical mapping demonstrates intense delamination in both samples, as well as the association of these regions with the O concentration.

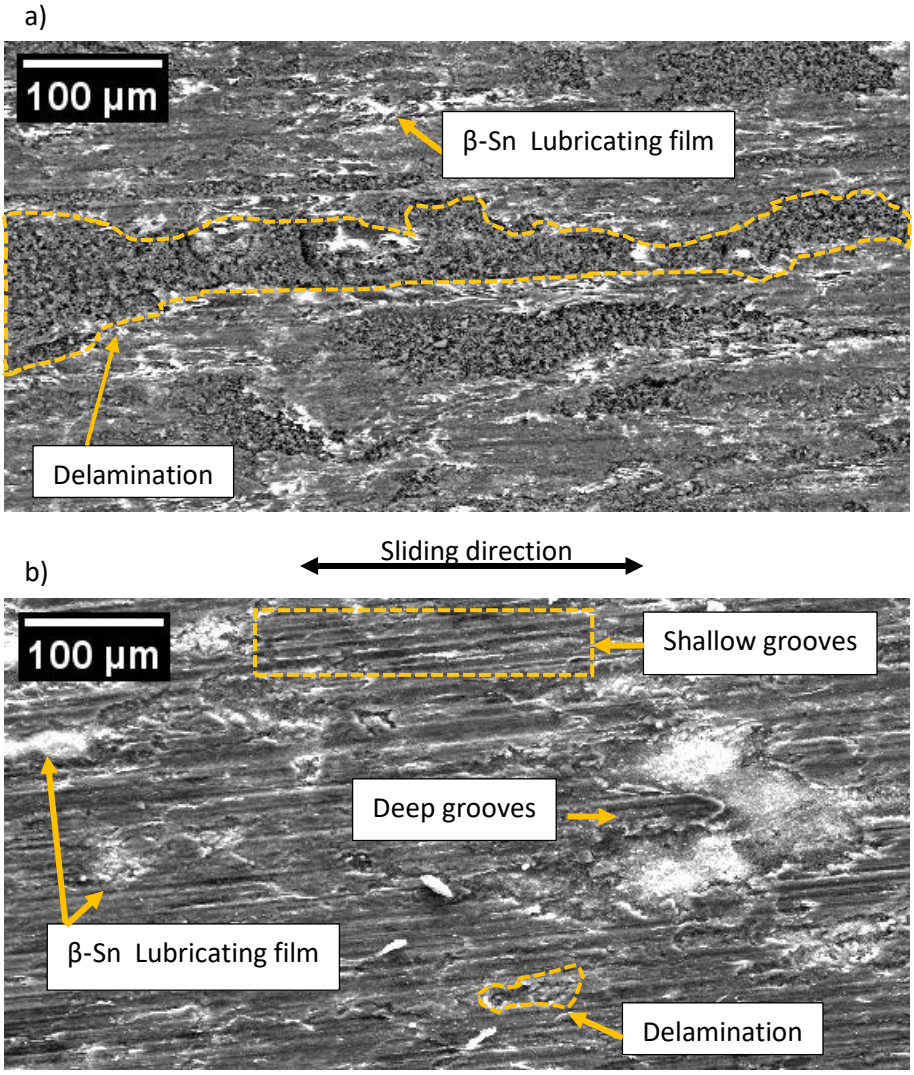

Figure 13 – SEM micrographs of the worn surfaces showing the different surface morphologies after 4,000 m of sliding distance and distinct microstructures: (a) λ_A = 15.7 µm and (b, d) λ_A = 49.5 µm.

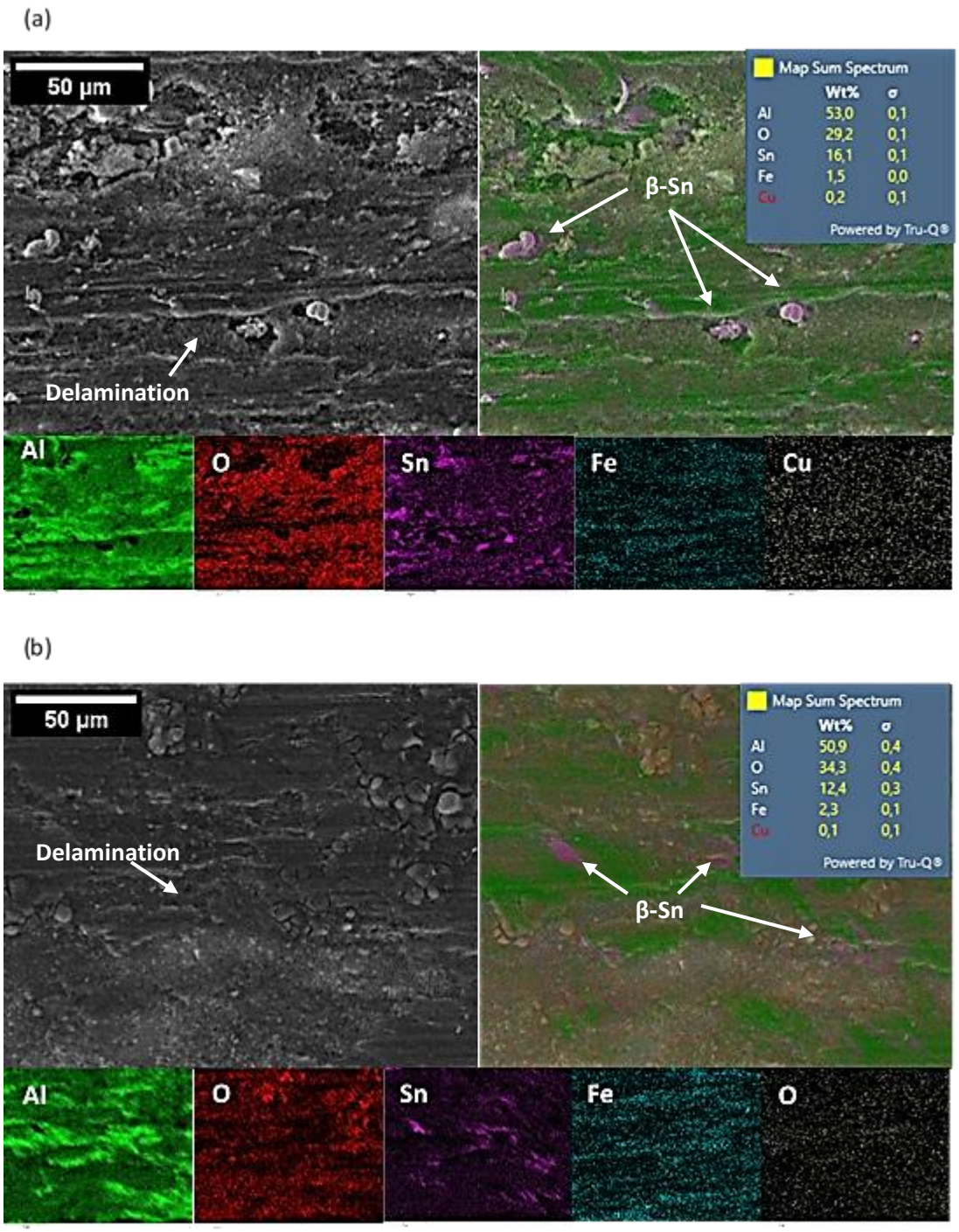

Figure 14 – SEM micrographs and EDS elemental maps of worn surfaces. The left images show the secondary electron images; the right top images display the superimposed elemental distribution maps of Al, O, Sn, Fe, and Cu. Individual elemental maps are shown as bottom images: (a) λ_A = 15.7 µm and (b) λ_A = 49.5 µm.

4. Discussion

The most important observation from these experiments is the variation in mechanical and tribological properties along the length of the ingot. Several mechanisms may be responsible for this phenomenon. These include the scale of the microstructure, the morphology of the β-Sn phase and the effects of macrosegregation. The following subsections will provide a detailed discussion of these features.

4.1. Influence of solidification conditions on cast microstructure

Upward unidirectional solidification experiments are commonly conducted for two main reasons: first, they enable the achievement of a wide range of cooling rates within a single experiment; second, they minimize the potential effects of liquid flow. However, in the case of the Al-20Sn-1Cu alloy, Sn tends to accumulate at the bottom of the ingot due to its higher density compared to Al. This macrosegregation lead to a non-uniform distribution of chemical composition within the ingot, as revealed by ICP analysis. Macrosegregation can occur in the processing of commercial alloys, such as those produced by chilled die casting. Furthermore, it cannot be eliminated through subsequent heat treatments [47].

The rejection of Sn, observed on a macroscopic scale, also influences the solidification at the microscale. As solidification proceeds, both Cu and Sn rejections occur at the solid/liquid interface, which lead to the formation of a solute-enriched layer that induces constitutional undercooling, destabilizing the planar solidification front [48]. When combined with the cooling rates observed in the experiment, this leads to the growth of α-Al dendrites, with Sn being trapped in the interdendritic regions [18,19,42]. This behavior is clearly illustrated in the SEM images shown in Figure 4 and further confirmed by the chemical analysis via EDS in Figure 5 and Table 2.

In a dendritic structure, the crystallographic direction plays a key role in determining the growth directions of the arms. In Al alloys, the preferred growth direction typically belongs to the <100> family [48], which forms six perpendicular branches [35]. However, as shown in previous studies with Al-Ge [49] and Al-Zn [50] alloys, dendrites oriented along the <110> direction can also grow in solute-rich Al-Sn

alloys [51,52]. Consequently, those dendrites have a greater number of branches and angles other than 90° between them, resulting in a more complex geometry, as seen in Figure 4 and similarly demonstrated in studies dealing with the Al-20 wt.% Sn alloys [25,53]. The quantification of the microstructure is rendered more complex, and consequently, an automatic method of measuring the average dendritic spacing per intersection has been proposed in this work.

In their studies on Al-Sn and Al-Sn-Cu alloys, Cruz *et al*. [22] and Bertelli *et al.* [45] successfully measured the primary dendritic spacing using the traditional triangular method and obtained the classical exponent of -0.55 to describe the power law relationship between the primary dendritic spacing and the cooling rate [54]. However, as shown in Figure 4, an exponent of -0.33 was found to be effective in describing the power law relationship for the present work. This finding indicates a more moderate influence of the cooling rate on the dendritic spacing. Potential explanations include the fact that these exponent accounts the DAS and so all types of spacing (primary, secondary, etc.), or reflects differences in the methods used to measure the dendritic spacing. The -0.33 exponent has also been employed in other multicomponent Al-based alloys subjected to unsteady-state solidification [25,55,56], although considering secondary dendritic spacings, which are also measured using the intercept method, similar to the approach employed in this work to determine the DAS.

Given the long solidification intervals characterizing Al-Sn alloys, cooling rates have a huge influence on the microstructure, not only on the microstructural coarsening, but also on the morphology of the β-Sn phase. As the α-Al phase grows in isolation over a temperature range of approximately 250 °C the Sn-rich liquid tends to sediment within the melt, under the influence of gravity. This motion is smoothed out and the coalescence of this liquid is reduced thanks to the α-Al dendritic arms. However, the more refined the microstructure, the more branched the dendritic arms become, increasing the complexity of the Sn phase network. As observed in the x-ray microtomography results (Figure 7), the variation in volume fraction among the most distinct samples is relatively small (<5%). In contrast, the difference in surface area is significantly more pronounced. Between the most extreme cooling conditions, the surface area of the Sn phase more than doubles, resulting in a substantially higher packing of the secondary phase.

4.2. Effect of microstructural morphology on the mechanical properties

In as-cast alloys strength improvement is achieved by the refinement of the dendritic microstructure, which ensures a weak microsegregation and a uniform distribution of second phases and other barriers to dislocation movement during slip [57]. However, in terms of microhardness, the Al-20Sn-1Cu alloy studied in this work showed an almost constant value of about 25 HV, regardless of the microstructural scale, as shown in Figure 8. The microhardness varied by about 4 HV between the maximum and minimum values, while the dendritic spacing almost tripled. This leads us to consider the effect of Sn macrosegregation on this property. It is worth noting that, during the hardness analyses, the indentations had a diagonal of approximately 180 μm, which included both the dendrites and the interdendritic regions, thus reflecting a combined behavior of all formed phases. And Sn, a soft metal with a low hardness (~7 HV, as measured in this study), appears to have a significant influence on the microhardness of the alloy, comparable to the impact of the microstructural scale, since a higher concentration of Sn leads to a reduction in the hardness of the alloy, even considering more refined microstructures.

Similar to the present work, Bertelli et al. [45] observed macrosegregation in upward solidified Al-20Sn-10Cu ingot and noted anomalous hardness behavior. The hardness was lower for smaller dendrite spacings at the bottom of the ingot which has a higher Sn content than the nominal composition (~32 wt.% Sn). Apart from this ingot region, the evolution of hardness with dendritic spacing followed the expected trend, i.e., hardness decreased as dendritic spacing increased. In [45], the hardness variation was more significant than in the present work, reflecting the more intense macrosegregation that occurs due to liquid phase separation in Al-Sn alloys with high Cu content, as well as the greater amount of copper, the strengthening element. In any case, it is confirmed that Sn content above 20 wt.% affects the hardness as much as the dendritic microstructural scale.

In a study of directionally solidified Al-20Sn alloy [22], it has been also observed macrosegregation levels comparable to those reported in [45], and they found that tensile properties are not influenced by Sn macrosegregation, as is evidenced in the present work. In the present work, there was an increase in strength

as the dendritic spacing decreased in all over ingot, culminating in superior strengths associated with the smaller average spacings cooled at higher cooling rate, particularly the 15.7 μm spacing at 28.9°C/s, as shown in Table 6. As noted by Campbell [58], finer dendritic arm spacing results in reducing microsegregation and enhancing stress and pore distribution, leading to better properties. Therefore, the cooling rate is a fundamental key to improving the microstructure, adapting the tensile properties of this alloy.

Surprisingly, both yield strength and elongation increased together. Thus, in addition to the dendritic spacing, another fundamental aspect to mechanical behavior understanding are the interfaces, even more between dendrite and phases. This issue was demonstrated by Ghassemali et al. [59] on as-cast Al-Si alloys, where most cracks were initiated at the dendrite/eutectic boundary, regardless of the grain boundary location. Indeed, the higher elemental segregation at the dendrite/eutectic boundaries compared to grain boundaries in cast alloys can introduce stress concentration at the dendritic boundaries interfering in the strain hardening and fracture mechanism.

Chemical analyses by EDS (Figure 5 and Table 4) reveal that the dendritic matrix and the interdendritic region consist of almost pure materials, respectively Al and Sn. Due to the significant differences in their mechanical behavior, the alloy can be classified as a hetero-structured material. As described in Ref. [60], under tensile loading, such a material undergoes HDI (hetero-deformation-induced) hardening. This occurs because the mechanical difference between the two phases during straining creates strain gradients at the interface.

To preserve the integrity of these boundaries during strain, many geometrically necessary dislocations (GNDs) accumulate near the interfaces in the β-Sn soft zone. This dislocation accumulation generates high back stress, which, in turn induces forward stress in the adjacent hard α-Al zone. As a result, internal stresses are formed at the interface, referred to as HDI stress. Importantly, as the deformation strain increases, so does the HDI stress. Thus, during plastic deformation, the interfaces between the hard and soft phases act as barriers to dislocation movement and therefore a dislocation transformation (e.g. slip) must

take place at these boundaries to continue strain. Consequently, larger interface areas can enhance the material mechanical properties by promoting a more effective strain hardening.

The microtomography analysis maps the Al matrix/Sn particles interface and its variation as a function of the cooling rate can be seen in Figure 7 and Table 5. It is observed that, a larger interface area between the Al matrix and Sn particles occurs in samples with a more refined structure as it has a larger surface area of the β-Sn phase and therefore with higher adherence. This justifies the combined improvement of ductility and strength for more refined dendritic arrays.

This explanation can be confirmed by analyzing the fractographs shown in Figure 11. When comparing the more refined sample and the coarser sample, it appears that there is a higher adhesion between the β-Sn particles and the α-Al dendritic matrix in the more refined sample (Figure 11 a), as there is no clear separation between the phases and there are signs of deformation throughout the fractography, including the presence of dimples (Figure 11 b). Under these conditions occurred a ductile fracture, which culminates in an improved strength and greater ductility (Figures 9, 10, and Table 6). Strain hardening exponent values also reinforces the argument of strain hardening by HDI, where higher values were estimated in the more refined microstructures. There is a sharp decrease in the *n* value as the dendritic spacing increases, concomitantly with the reduction in the surface area of β-Sn and, therefore, in the adhesion of the α-Al and β-Sn phases. The fractographs in Figure 11 c) and d), as well as the typical stress-strain curves shown in Figure 9 and the tensile properties shown in Figure 10 and Table 6, make us believe that a decohesive brittle fracture in the interdendritic region is associated with the coarser microstructures (Figure 11 c and d).

When the volumetric fraction of the β-Sn soft phase is too high to be fully constrained by the hard phase, it will undergo plastic deformation under lower applied stress, resulting in reduced yield strength and rupture at the interface as seen in Figure 11c. As a variation occurs in the morphology and, consequently, in the adhesion of β-Sn to the α-Al matrix, the variation in the tensile strength and ductility curves observed in Figure 10 can be seen.

4.3. Influence of microstructural morphology on the wear behavior

Considering the microhardness data shown in Figure 8, it can be observed that the two samples associated with the microstructural conditions subjected to wear test (that is, finer sample λ_A= 15.7 μm and coarser sample λ_A= 49.5 μm) exhibit very similar hardness values, i.e., ~25 HV, which explains the difference in the wear results solely by the β-Sn phase morphology and distribution. Thus, the Archard equation, which implies volume loss decreases as hardness and strength increase [7], does not fully capture the wear behavior, making the dimensional wear coefficient a more suitable parameter for understanding this alloy. This conclusion is supported by the dimensional wear coefficient as a function of sliding distance graph, as shown in Figure 12, with clearly different trend lines for each sample, within the same order of magnitude, with the coarser sample having the best wear resistance.

The volume of material worn from both samples initially increased sharply until reaching a state of relative equilibrium (Figure 12). This phenomenon can be attributed to the tribological behavior of materials under dry sliding contact, as observed in other wear studies on Al alloys [13,19,25]. This phenomenon can be justified by the fact that during the initial contact between the rolling ball and the flat sample, adhesive wear occurs, characterized by a high wear rate and intense surface damage. As the experiment progresses, the interaction between the removed material and the existing phases prompts a transition in the wear mechanism, potentially resulting in a reduction in the rate of volume removed, eventually stabilizing at a lower and more consistent value.

Indeed, the topography of the worn surface and the EDS chemical map (see Figures 13 and 14) indicate the presence of multiple wear mechanisms in both alloys. This finding is consistent with the observations reported in previous studies of aluminum alloys subjected to dry contact wear [12,24,25]. As indicated by [12–14,25], the progression of wear mechanisms in the context of soft alloys unfolds as described below: At the initial point of contact, the soft phase is pulled towards the surface. These particles then cover the worn surface, forming a solid lubricant film. However, failure or inefficiency of this film may lead to direct contact between the worn surface and the rotating element, causing adhesive wear, and removing a large volume of material. As sliding continues, material removed during the adhesive wear

stage adheres to the ball, creating abrasive particles that contribute to abrasive wear and other wear mechanisms are also possible as sliding progress.

In self-lubricating alloys, the wear behavior is largely attributed to the soft phase, its quantity and distribution. By comparing the chemical map and SE-SEM images of the worn surfaces of the two samples tested (Figure 13), it was identified that only in the coarser sample did the β-Sn phase have a ground appearance, consistent with what is expected to form a protective film. In the more refined sample, β-Sn was present in higher quantities, but with a rigid and preserved morphology. According to the microtomography results (Figure 7 and Table 5), the refined sample presents a higher Sn surface area, which should favor the formation of the lubricating layer, however the wear results suggest the opposite. Perhaps the complexity of the refined network, where the Sn phase is well adhered to the Al matrix, makes it difficult to knead it towards the worn surface. Considering abrasive wear as the initial stage and the one responsible for removing large volumes of material, the low efficiency in the formation of the protective film of the more refined sample reflects its higher dimensional wear coefficient, corroborated by the intense delamination marks shown in the SEM images (Figure 13 and 14).

The presence of Fe on the worn surfaces was identified, indicating that dry contact conditions occurred due to insufficient lubricating effect of Sn in certain regions. Fragments from the steel ball adhered to and later detached from the surface, suggesting wear by adhesion through material transfer or abrasion when the detachment of harder particles begins to act as a third-body abrasive. The Fe content was slightly higher in the coarser sample. Additionally, chemical mapping revealed a high presence of oxygen (29.2%, 32.3%), especially in the coarser sample. The heat generated by plastic deformation—particularly in Sn-rich particles—combined with the reaction between atmospheric oxygen and the contact region, led to the formation of an oxide layer [25], most likely aluminum oxide (Al_2O_3). The oxide formation was mainly concentrated in the delaminated regions, which were torn off due to the inefficiency of the Sn solid lubricant layer coverage, as seen in the SE images (Figure 13 and 14). The results indicated multiple wear mechanisms: oxidative, adhesive, and abrasive

The existence of an oxide layer on the worn surface can have detrimental or beneficial effects on wear, depending on the alloy system and the wear conditions. The oxide layer formed on the worn surface can compete with the solid lubricant layers, potentially reducing the effectiveness of the lubrication. In addition, the oxide layer can become brittle and promote the detachment of hard particles that can act as third wear bodies [10,12,13,23,25]. However, in certain cases, a stable oxide layer can have positive effects, as observed in the studies by [9] and [61] with Al2024 alloys reinforced with B4C composites and Al-Si reinforced with Si/Cp, respectively.

As demonstrated by the dimensional wear coefficient curves as a function of distance, the coarser sample exhibited higher resistance to wear, although the formation of the oxidation layer was more significant. While numerous studies have previously considered oxidation to be detrimental, this was not observed in the present work under the conditions investigated. Further studies are required to elucidate the function of the oxidative layer under varied loading conditions and temporal variations

Although the finer dendritic microstructure is not as effective in wear as it is in properties like ductility and tensile strength, this behavior has been observed in other self-lubricating Al alloys with soft second phases such as Sn [22,25,45], In [14], and Pb [3], since these elements have extremely low hardness and similar wear mechanisms. The measure of wear provided by *k* is particularly useful for comparing wear rates in different materials, allowing comparisons with the literature. In order to compare the wear behavior of the alloy studied in this work with that of other alloys described in the literature, the dimensional wear coefficient was calculated for different alloys, using information on load and wear volume provided by the studies [3,12,14,22] and presented in Figure 15. For this comparison, the same DAS of 15.7 μm was considered, corresponding to the worst condition observed in this work. The comparison of wear coefficient data in Figure 15 with other self-lubricating alloys from the literature is, to some extent, encouraging, since it exhibited a lower wear coefficient compared to many other tested alloys. Furthermore, after a certain distance of approximately 2,000 meters of wear, the Al-20Sn-1Cu alloy exhibited stabilization in its wear behavior, which is most likely due to the formation of a stable tribological layer. This warrants future studies for further understanding on its composition and nature. The alloy from the literature [12] with a higher

copper content was the only one that outperformed the alloy of interest. This is due to the higher copper content in solid solution, which increased the alloy hardness and, consequently, slightly reduced its wear coefficient.

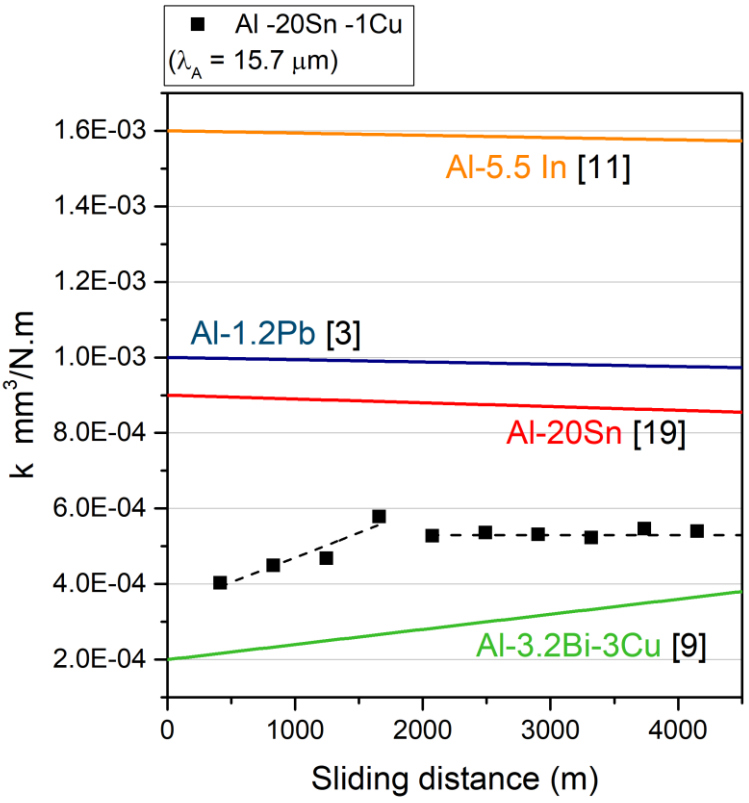

Figure 15 – Comparison between the dimensional wear coefficient as a function of the sliding distance of the more refined sample (λ_A=15.7 μm) produced with the Al-20Sn-1Cu alloy in this study and other studies in the literature.

5. Conclusions

The following conclusions can be drawn from the present findings:

- The upward unidirectional solidification technique enables precise control over cooling rates, resulting in varied microstructures across the ingot. Macrosegregation, a key defect in the Al-20Sn-1Cu alloy, arises due to density differences between Al and Sn, causing Sn to accumulate at the bottom of the

ingot. This phenomenon significantly influences both macro- and microstructural features, such as solute distribution and dendritic morphology. Higher cooling rates promote finer dendritic structures, which enhance the homogeneity of solute trapping and reduce the severity of macrosegregation. Moreover, a -0.33-power function exponent has been employed to correlate DAS with the solidification cooling rate using the dendritic arm spacing measuring methodology proposed in the present paper.

- Mechanical properties in the Al-20Sn-1Cu alloy are demonstrated to be strongly tied to microstructural features, particularly dendritic spacing and β-Sn phase distribution. Finer dendritic arrays, formed under higher cooling rates, improve strength and ductility by promoting strain hardening and obstacles to the dislocation movement at the α-Al/β-Sn interfaces. However, the microhardness remains relatively unchanged, which is attributed to the high Sn content in the alloy. The soft β-Sn phase significantly influences hardness and tensile deformation behavior, with its hetero-deformation-induced (HDI) hardening effect being prominent. Coarser dendritic microstructures with larger Sn regions result in reduced strength and ductility, highlighting the importance of microstructure refinement in optimizing mechanical properties of a self-lubricating alloy.
- The wear behavior of the Al-20Sn-1Cu alloy is predominantly influenced by the size, morphology, and distribution of the β-Sn phase, despite similar hardness across different microstructures. Coarser dendritic structures, with larger and more spherical Sn regions, enhance lubrication effects by forming stable interfacial layers during wear, reducing the wear coefficient. The dimensional wear coefficient comparison indicates that the alloy performs favorably against other self-lubricating alloy systems, with wear behavior stabilizing after the formation of a tribological layer.

Acknowledgements

The authors are grateful to CNPq—National Council for Scientific and Technological Development, Brazil and to FAPESP—São Paulo Research Foundation, Brazil (grant numbers 2023/06107-3 and 2023/03242-7) for their financial support. This study was financed in part by the Coordenação de Aperfeiçoamento de Pessoal de Nível Superior—Brasil (CAPES)—Finance Code 001. We are grateful to the Brazilian Nanotechnology National Laboratory (LNNano), part of the Brazilian Centre for Research in Energy and Materials (CNPEM), and to the support from the Mogno beamline staff during the Micro-CT experiments in the frame of the project #20232581.

Data Availability Statement

Data presented in this study are available on request from the corresponding author.

References

[1] M.M. Khonsari, E.R. Booser, Applied Tribology: Bearing Design and Lubrication, 3rd Editio, Wiley, 2017.

[2] Z.M. Wang, Q. Yang, Z.P. Sun, B.R. Zhang, W. Zhao, W.F. Rao, The effects of Bi and Pb on the soft phase in Al82Sn15Si2.2Cu0.8 sliding bearing alloy, Mater. Charact. 170 (2020) 110684. https://doi.org/10.1016/j.matchar.2020.110684.

[3] E.S. Freitas, A.P. Silva, J.E. Spinelli, L.C. Casteletti, A. Garcia, Inter-relation of microstructural features and dry sliding wear behavior of monotectic al-bi and al-pb alloys, Tribol. Lett. 55 (2014) 111–120. https://doi.org/10.1007/s11249-014-0338-8.

[4] R. Schouwenaars, V.H. Jacobo, A. Ortiz, Microstructural aspects of wear in soft tribological alloys, Wear. 263 (2007) 727–735. https://doi.org/10.1016/j.wear.2006.12.037.

[5] N.A. Bushe, I.G. Goryacheva, Y.Y. Makhovskaya, Effect of aluminum-alloy composition on self-lubrication of frictional surfaces, Wear. 254 (2003) 1276–1280. https://doi.org/10.1016/S0043-1648(03)00110-8.

[6] A.E. Bravo, H.A. Durán, V.H. Jacobo, A. Ortiz, R. Schouwenaars, Towards new formulations for journal bearing alloys, Wear. 302 (2013) 1528–1535. https://doi.org/10.1016/j.wear.2013.01.040.

[7] M. Beder, S.B. Akçay, T. Varol, H. Çuvalcı, The Effect of Heat Treatment on the Mechanical Properties and Oxidation Resistance of AlSi10Mg Alloy, Arab. J. Sci. Eng. 49 (2024) 15335–15346. https://doi.org/10.1007/s13369-024-08971-1.

[8] M. Beder, T. Varol, S.B. Akçay, H. Çuvalcı, F. Erdemir, M.A. Khan, U.T. Yıldız, The effect of high SiC ratio on the physical, mechanical, tribological and corrosion behavior of Al2024 alloy matrix composites fabricated by powder metallurgy, J. Compos. Mater. 0 (2025) 1–23. https://doi.org/10.1177/00219983251316237.

[9] M. Beder, The effect of high B4C ratio on the improvement of mechanical properties and wear resistance of Al2024/B4C composites fabricated by mechanical milling-assisted hot pressing, Ceram. Int. 51 (2025) 9528–9547. https://doi.org/10.1016/j.ceramint.2025.01.287.

[10] M. Beder, T. Varol, S.B. Akçay, Impact of high Al2O3 content on the microstructure, mechanical properties, and wear behavior Al–Cu–Mg/Al2O3 composites prepared by mechanical milling, Ceram. Int. 50 (2024) 38610–38631. https://doi.org/10.1016/j.ceramint.2024.07.230.

[11] M.Â.O. de Alfaia, R. Oliveira, T.S. Lima, F.E. Mariani, L.C. Casteletti, N. Cheung, A. Garcia, Effects of cooling rate and microstructure scale on wear resistance of unidirectionally solidified Al-3.2wt.%Bi-(1; 3) wt.%Pb alloys, Mater. Today Commun. 25 (2020). https://doi.org/10.1016/j.mtcomm.2020.101659.

[12] R. V. Reyes, V.E. Pinotti, C.R.M. Afonso, L.C. Casteletti, A. Garcia, J.E. Spinelli, Processing, As-Cast Microstructure and Wear Characteristics of a Monotectic Al-Bi-Cu Alloy, J. Mater. Eng. Perform. 28 (2019) 1201–1212. https://doi.org/10.1007/s11665-018-3851-3.

[13] T.A. Costa, M. Dias, E.S. Freitas, L.C. Casteletti, A. Garcia, The effect of microstructure length scale on dry sliding wear behaviour of monotectic Al-Bi-Sn alloys, J. Alloys Compd. 689 (2016) 767–776. https://doi.org/10.1016/j.jallcom.2016.08.051.

[14] E.S. Freitas, J.E. Spinelli, L.C. Casteletti, A. Garcia, Microstructure-wear behavior correlation on a directionally solidified Al-In monotectic alloy, Tribol. Int. 66 (2013) 182–186. https://doi.org/10.1016/j.triboint.2013.05.009.

[15] T. Tamura, M. Li, K. Takahashi, E. Inoue, Improved solidification structures and mechanical properties of Al–20 wt% Sn alloys processed by an electromagnetic vibration technique, Mater. Sci. Eng. A. 862 (2023). https://doi.org/10.1016/j.msea.2022.144416.

[16] F. Bertelli, E.S. Freitas, N. Cheung, M.A. Arenas, A. Conde, J. de Damborenea, A. Garcia, Microstructure, tensile properties and wear resistance correlations on directionally solidified Al-Sn-(Cu; Si) alloys, J. Alloys Compd. 695 (2017) 3621–3631. https://doi.org/10.1016/j.jallcom.2016.11.399.

[17] Z.C. Lu, M.Q. Zeng, Y. Gao, J.Q. Xing, M. Zhu, Improving wear performance of dual-scale Al-Sn alloys by adding nano-Si@Sn: Effects of Sn nanophase lubrication and nano-Si polishing, Wear. 338–339 (2015) 258–267. https://doi.org/10.1016/j.wear.2015.06.017.

[18] X. Liu, M.Q. Zeng, Y. Ma, M. Zhu, Promoting the high load-carrying capability of Al-20wt%Sn bearing alloys through creating nanocomposite structure by mechanical alloying, Wear. 294–295 (2012) 387–394. https://doi.org/10.1016/j.wear.2012.07.021.

[19] X. Liu, M.Q. Zeng, Y. Ma, M. Zhu, Wear behavior of Al-Sn alloys with different distribution of Sn dispersoids manipulated by mechanical alloying and sintering, Wear. 265 (2008) 1857–1863. https://doi.org/10.1016/j.wear.2008.04.050.

[20] H.R. Kotadia, E. Doernberg, J.B. Patel, Z. Fan, R. Schmid-Fetzer, Solidification of Al-Sn-Cu based immiscible alloys under intense shearing, Metall. Mater. Trans. A Phys. Metall. Mater. Sci. 40 (2009) 2202–2211. https://doi.org/10.1007/s11661-009-9918-x.

[21] Z.C. Lu, M.Q. Zeng, Y. Gao, M. Zhu, Minimizing tribolayer damage by strength-ductility

matching in dual-scale structured Al-Sn alloys: A mechanism for improving wear performance, Wear. 304 (2013) 162–172. https://doi.org/10.1016/j.wear.2013.05.001.

[22] K.S. Cruz, E.S. Meza, F.A.P. Fernandes, J.M.V. Quaresma, L.C. Casteletti, A. Garcia, Dendritic Arm Spacing Affecting Mechanical Properties and Wear Behavior of Al-Sn and Al-Si Alloys Directionally Solidified under Unsteady-State Conditions, Metall. Mater. Trans. A. 41 (2010) 972–984. https://doi.org/10.1007/S11661-009-0161-2.

[23] B.P. Reis, M.M. Lopes, A. Garcia, C.A. dos Santos, The correlation of microstructure features, dry sliding wear behavior, hardness and tensile properties of Al-2wt%Mg-Zn alloys, J. Alloys Compd. 764 (2018) 267–278. https://doi.org/10.1016/j.jallcom.2018.06.075.

[24] T.M. Botelho, H.M. Azevedo, G.H. Machado, C.R. Barbosa, F.S. Rocha, T.A. Costa, O.L. Rocha, Effect of solidification process parameters on dry sliding wear behavior of AlNiBi alloy, Trans. Nonferrous Met. Soc. China (English Ed. 30 (2020) 582–594. https://doi.org/10.1016/S1003-6326(20)65237-2.

[25] A. Barros, C. Cruz, T. Botelho, A. Silva, L. Casteletti, A. Garcia, N. Cheung, Dry Sliding Wear Features of an Al-20Sn-5Zn Alloy Affected by Microstructural Length Scales, Lubricants. 10 (2022). https://doi.org/10.3390/lubricants10120352.

[26] N.A. Belov, T.K. Akopyan, I.S. Gershman, O.O. Stolyarova, A.O. Yakovleva, Effect of Si and Cu additions on the phase composition, microstructure and properties of Al-Sn alloys, J. Alloys Compd. 695 (2017) 2730–2739. https://doi.org/10.1016/j.jallcom.2016.11.193.

[27] D. Mirković, J. Gröbner, R. Schmid-Fetzer, Liquid demixing and microstructure formation in ternary Al-Sn-Cu alloys, Mater. Sci. Eng. A. 487 (2008) 456–467. https://doi.org/10.1016/j.msea.2007.10.043.

[28] S.M. de Albuquerque Sousa, G.L. de Gouveia, J.E. Spinelli, Evaluating grain size, dendritic scale, and tensile properties of a NbB-inoculated 6201 alloy using solidification rate, Mater. Sci. Eng. A. 835 (2022) 142680. https://doi.org/10.1016/J.MSEA.2022.142680.

[29] F.A. Souza, I.A. Magno, M.O. Costa, A.S. Barros, J.M. Nascimento, D.B. Carvalho, O.L. Rocha, Unsteady-State Horizontal Solidification of an Al–Si–Cu–Fe Alloy: Relationship Between Thermal Parameters and Microstructure with Mechanical Properties/Fracture Feature, Met. Mater. Int. 25 (2019) 18–33. https://doi.org/10.1007/s12540-018-0174-8.

[30] A. S. Cooper, Precise lattice constants of germanium, aluminum, gallium arsenide, uranium, sulphur, quartz and sapphire, Acta Cryst. 15 (1962) 578–582.

[31] H.F. Swanson, E. Tatge, Standard X-Ray Diffraction Powder Patterns, Natl. Bur. Stand. Circ. 539. 1 (1953).

[32] L.. Razin, L.V., Rudashevskij, N.S., and Vyalsov, New natural intermetallic compounds of aluminium, copper and zinc—khatyrkite CuAl2, cupalite, CuAl and zinc aluminides—from hyperbasites of dunite-harzburgite formation, 1985. (n.d.).

[33] C.A. Schneider, W.S. Rasband, K.W. Eliceiri, NIH Image to ImageJ: 25 years of image analysis, Nat. Methods. 9 (2012) 671–675. https://doi.org/10.1038/nmeth.2089.

[34] T. Ferreira, W. Rasband, ImageJ User Guide IJ 1.46r, Image J User Guid. (2012). https://doi.org/10.1038/nmeth.2019.

[35] M. Gündüz, E. Çadirli, Directional Solidification of Aluminium–Copper Alloys, Mater. Sci. Eng. A. 327 (2002) 167–185. https://doi.org/10.1016/S0921-5093(01)01649-5.

[36] ASTM International ASTM E112-13, ASTM E112-13 Standard Test Methods for Determining Average Grain Size, (2014).

[37] I. Arganda-Carreras, V. Kaynig, C. Rueden, K.W. Eliceiri, J. Schindelin, A. Cardona, H.S. Seung, Trainable Weka Segmentation: A machine learning tool for microscopy pixel classification, Bioinformatics. 33 (2017) 2424–2426. https://doi.org/10.1093/bioinformatics/btx180.

[38] ASTM International, ASTM E8 / E8M - 21 Standard Test Methods for Tension Testing of Metallic Materials, (2021). https://doi.org/10.1520/E0008_E0008M-21.

[39] S.K. Kang, Y.C. Kim, K.H. Kim, D. Kwon, J.Y. Kim, Constitutive equations optimized for determining strengths of metallic alloys, Mech. Mater. 73 (2014) 51–57. https://doi.org/10.1016/j.mechmat.2014.01.010.

[40] D.A. de Moura, L.F. Gomes, C.A. Siqueira, A. Garcia, J.E. Spinelli, Understanding solidification and wear behaviour of Al-3Cu-Bi alloys, Mater. Sci. Technol. 39 (2023) 694–704. https://doi.org/10.1080/02670836.2022.2132733.

[41] I.M. Hutchings, Tribology — Friction and wear of engineering materials, 1992. https://doi.org/10.1016/0301-679x(92)90040-t.

[42] H. Jung, N. Mangelinck-Noël, H. Nguyen-Thi, B. Billia, Columnar to equiaxed transition during directional solidification in refined Al-based alloys, J. Alloys Compd. 484 (2009) 739–746. https://doi.org/10.1016/j.jallcom.2009.05.029.

[43] L. Abou-Khalil, K.S. da Cruz, G. Reinhart, N. Mangelinck-Noël, H. Nguyen-Thi, Influence of growth velocity on fragmentation during directional solidification of Al – 14 wt.% Sn alloy studied by in-situ synchrotron X-radiography, Acta Mater. 241 (2022) 118370. https://doi.org/10.1016/j.actamat.2022.118370.

[44] C.A. Gandin, Experimental study of the transition from constrained to unconstrained growth during directional solidification, ISIJ Int. 40 (2000) 971–979. https://doi.org/10.2355/isijinternational.40.971.

[45] F. Bertelli, C. Brito, I.L. Ferreira, G. Reinhart, H. Nguyen-Thi, N. Mangelinck-Noël, N. Cheung, A. Garcia, Cooling thermal parameters, microstructure, segregation and hardness in directionally solidified Al-Sn-(Si;Cu) alloys, Mater. Des. 72 (2015) 31–42. https://doi.org/10.1016/j.matdes.2015.02.006.

[46] B. Dong, Z. Wu, P. Wang, C. Ke, S. Liu, J. Jie, CALPHAD-guided alloy design of Bi-modified Al–Sn bearing alloy with multiphase composite structure and optimal self-lubricating property, J. Alloys Compd. 874 (2021). https://doi.org/10.1016/j.jallcom.2021.159756.

[47] R. Nadella, D.G. Eskin, Q. Du, L. Katgerman, Macrosegregation in direct-chill casting of aluminium alloys, Prog. Mater. Sci. 53 (2008) 421–480. https://doi.org/10.1016/j.pmatsci.2007.10.001.

[48] W. Kurz, D.J. Fisher, Fundamentals of Solidification, in: 4th ed., Trans Tech Publications, Switzerland, 1986: p. 316.

[49] M. Becker, J.A. Dantzig, M. Kolbe, S.T. Wiese, F. Kargl, Dendrite orientation transition in Al–Ge alloys, Acta Mater. 165 (2019) 666–677. https://doi.org/10.1016/j.actamat.2018.12.001.

[50] J. Friedli, J.L. Fife, P. Di Napoli, M. Rappaz, Dendritic growth morphologies in Al-Zn alloys - Part I: X-ray tomographic microscopy, Metall. Mater. Trans. A Phys. Metall. Mater. Sci. 44 (2013) 5522–5531. https://doi.org/10.1007/s11661-013-1912-7.

[51] R.E. Napolitano, S. Liu, Three-dimensional crystal-melt Wulff-shape and interfacial stiffness in the Al-Sn binary system, Phys. Rev. B - Condens. Matter Mater. Phys. 70 (2004) 1–11. https://doi.org/10.1103/PhysRevB.70.214103.

[52] G. Reinhart, F. Ngomesse, F. Bertelli, P. Benigni, A. Campos, H. Nguyen-Thi, Investigation of Al-20Sn-10Cu alloy directional solidification by laboratory X-radiography, IOP Conf. Ser. Mater. Sci. Eng. 1274 (2023) 012054. https://doi.org/10.1088/1757-899x/1274/1/012054.

[53] K.S. Cruz, J.E. Spinelli, I.L. Ferreira, N. Cheung, A. Garcia, Microstructural development in Al-Sn alloys directionally solidified under transient heat flow conditions, Mater. Chem. Phys. 109 (2008) 87–98. https://doi.org/10.1016/j.matchemphys.2007.10.037.

[54] J.E. Spinelli, N. Cheung, A. Garcia, On array models theoretical predictions versus measurements for the growth of cells and dendrites in the transient solidification of binary alloys, Philos. Mag. 91 (2011) 1705–1723. https://doi.org/10.1080/14786435.2010.545779.

[55] C. Brito, T.A. Costa, T.A. Vida, F. Bertelli, N. Cheung, J.E. Spinelli, A. Garcia, Characterization of Dendritic Microstructure, Intermetallic Phases, and Hardness of Directionally Solidified Al-Mg and Al-Mg-Si Alloys, Metall. Mater. Trans. A Phys. Metall. Mater. Sci. 46 (2015) 3342–3355. https://doi.org/10.1007/s11661-015-2967-4.

[56] R. Kakitani, C. Konno, A. Garcia, N. Cheung, The Effects of Solidification Cooling and Growth Rates on Microstructure and Hardness of Supersaturated Al-7%Si-x%Zn Alloys, J. Mater. Eng. Perform. 31 (2022) 1956–1970. https://doi.org/10.1007/s11665-021-06341-8.

[57] J.A. Dantzig, M. Rappaz, Solidification - Revised & Expanded, 2th editio, EPFL Press English Imprint, 2016.

[58] J. Campbell, Casting, Butterworth-Heinemann, 2003.

[59] E. Ghassemali, M. Riestra, T. Bogdanoff, B.S. Kumar, S. Seifeddine, Hall-Petch Equation in a Hypoeutectic Al-Si Cast Alloy: Grain Size vs. Secondary Dendrite Arm Spacing, Procedia Eng. 207 (2017) 19–24. https://doi.org/10.1016/J.PROENG.2017.10.731.

[60] X. Dong, B. Gao, L. Xiao, J. Hu, M. Xu, Z. Li, J. Meng, X. Han, H. Zhou, Y. Zhu, Heterostructured Metallic Structural Materials: Research Methods, Properties, and Future Perspectives, Adv. Funct. Mater. 2410521 (2024) 1–34. https://doi.org/10.1002/adfm.202410521.

[61] X.Y. Li, K.N. Tandon, Microstructural characterization of mechanically mixed layer and wear debris in sliding wear of an Al alloy and an Al based composite, Wear. 245 (2000) 148–161. https://doi.org/10.1016/S0043-1648(00)00475-0.

[62] Trainable Weka Segmentation, (n.d.). https://imagej.net/plugins/tws/ (accessed January 29, 2025).

Appendix A

In order to automatically measure the DAS, the micrographs need to be segmented into two regions of interest: the dendritic region and the interdendritic region. To do this, the “Trainable Weka Segmentation” (TWS) plug-in is used, which is an advanced tool for image segmentation. TWS allows

supervised segmentation, in which the user provides examples of regions of interest (ROI) so that the algorithm can learn the characteristics of these areas and then apply this knowledge to new images.

The TWS training process involves the user selecting representative samples of each class (in this case, the dendritic and interdendritic regions) so that the model can learn to distinguish between these areas based on texture, color and pixel intensity characteristics. After training, the model can automatically segment similar images, assigning labels to the pixels based on the classes learned.

Images A1a) and A1b) show the original image and the segmented image, respectively. In the segmented image (A1a), the green color represents the interdendritic region, while the red color corresponds to the dendritic region. Figure A1c shows a superimposed comparison between the original image and the segmented image, showing that the segmentation process was effective in separating the two regions of interest, with a good correspondence between the delimited areas and the expected regions. The segmentation was carried out accurately, demonstrating the effectiveness of the method used in discriminating between the different regions of the image.

For more information on how to use “Trainable Weka Segmentation” and configure segmentation training, see the detailed documentation available at [37] [62].

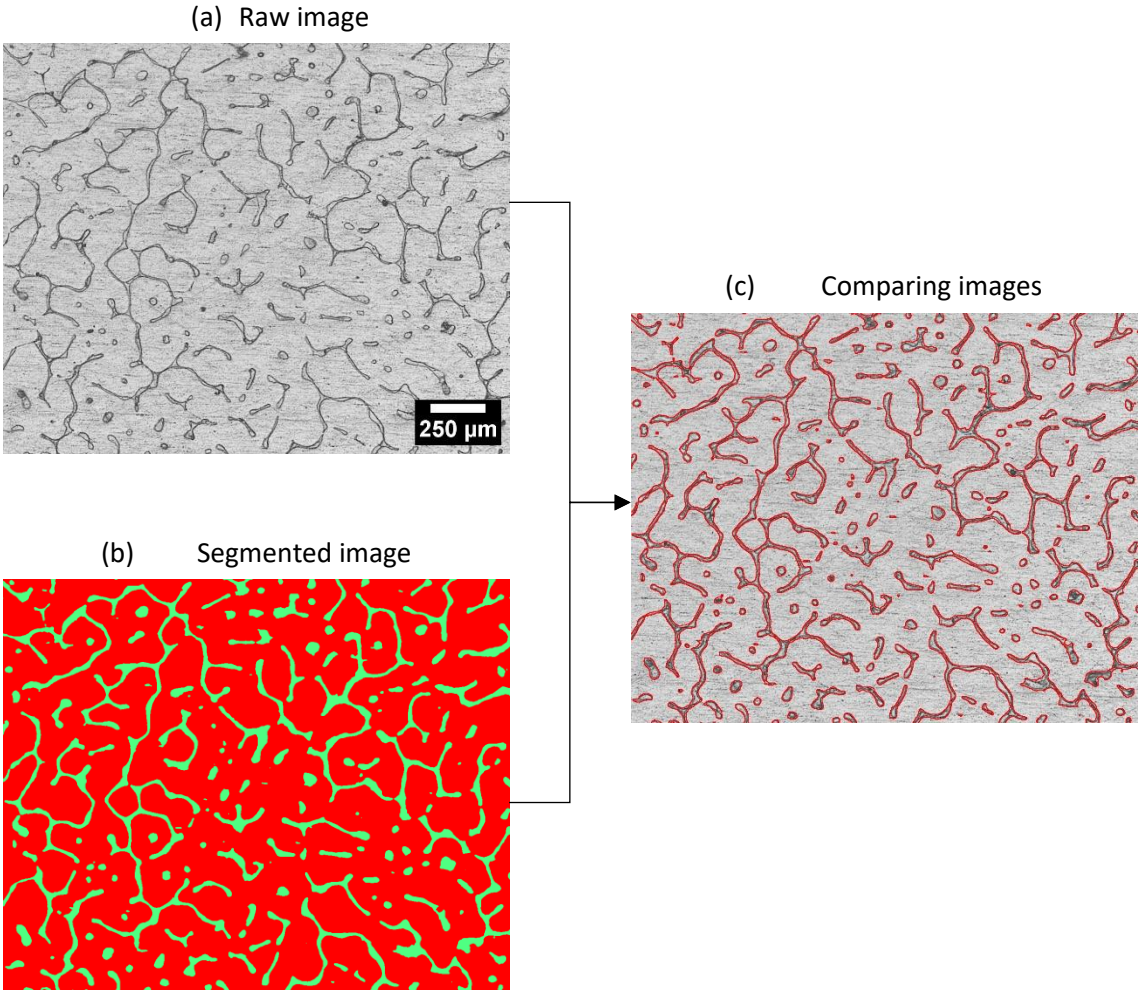

Figure A1 - Segmentation of the micrograph using the WTS tool. a) the original image, b) the image segmented into two regions, the dendritic region in red and the interdendritic region in green, c) the comparison between the original image and the segmented image with the interdendritic regions delimited in red.

After segmentation, the DAS can be accurately calculated by binarizing the image using thresholding. Binarization transforms the image into two classes of pixels: one class representing the dendrites (white) and the other representing the interdendritic region (black), as shown in Figure A2.

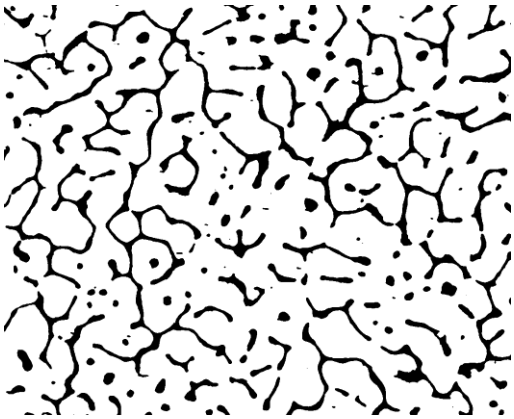

Figure A2 - Binarized figure. In white, the dendritic region and in black, the interdendritic region.

The DAS is calculated using a macro created in ImageJ. The macro is saved as a text file and executed from the ImageJ menu. The process consists of drawing ‘n’ lines on the micrograph and, for each one, counting the number of intersections with the interdendritic regions. The ratio between the length of the line and the number of intersections is then calculated. The images are analysed in pixel units. After calculating the dendritic spacing (DAS), the value obtained must be converted to micrometers, using the original scale of the micrograph.

The command script used for this task is described below:

```
////////////////////////////////////////////////
// Require a binary image.
// Boundaries are black.
////////////////////////////////////////////////


H = getHeight();
W = getWidth();

x1 = 0;
x2 = W;
y1 = 0;
y2 = H;

////////////////////////////////////////////////
//User specifies the number of lines to be cleated
////////////////////////////////////////////////
```

```
Dialog.create("Number of lines");
Dialog.addSlider("N", 1, 1000, 100);
Dialog.show();
N = Dialog.getNumber();

for (j = 0; j < N; j++)
{

    ////////////////////////////////////////////////////////////////
    //Draw a line from one side of the image to the other at random.
    ////////////////////////////////////////////////////////////////
    X_or_Y = random;

    ////////////////////////////////////////
    //Line drawn from left end to right end
    ////////////////////////////////////////
    if (X_or_Y <= 0.166)
    {
        x1 = 0;
        y1 = random * H;
        x2 = W;
        y2 = random * H;
        makeLine(x1, y1, x2, y2);
    }


    ////////////////////////////////////////
    //Line drawn from left end to top end
    ////////////////////////////////////////
    if (X_or_Y > 0.166 && X_or_Y <=0.333)
    {
        x1 = 0;
        y1 = random * H;
        x2 = random *W;
        y2 = H;
        makeLine(x1, y1, x2, y2);
    }
    ////////////////////////////////////////
    //Line drawn from left end to bottom end
    ////////////////////////////////////////
    if (X_or_Y > 0.333 && X_or_Y <=0.5)
    {
        x1 = 0;
        y1 = random * H;
        x2 = random *W;
```

```
        y2 = 0;
        makeLine(x1, y1, x2, y2);
    }
    ////////////////////////////////////////
    //Line drawn from bottom end to top end
    ////////////////////////////////////////
    if (X_or_Y > 0.5 && X_or_Y <=0.666)
    {
        x1 = random *W;
        y1 = 0;
        x2 = random *W;
        y2 = H;
        makeLine(x1, y1, x2, y2);
    }
    ////////////////////////////////////////
    //Line drawn from bottom end to right end
    ////////////////////////////////////////
    if (X_or_Y > 0.666 && X_or_Y <=0.833)
    {
        x1 = random *W;
        y1 = 0;
        x2 = W;
        y2 = random*H;
        makeLine(x1, y1, x2, y2);
    }
    ////////////////////////////////////////
    //Line drawn from right end to top end
    ////////////////////////////////////////
    if (X_or_Y > 0.833 && X_or_Y <=1)
    {
        x1 = W;
        y1 = random * H;
        x2 = random*W;
        y2 = H;
        makeLine(x1, y1, x2, y2);
    }

    ////////////////////////////////////////////////////////////////////////////////
////////////////
    //Calculate the number of crossed boundaries. White pixels value = 255, black
pixels value=0
    ////////////////////////////////////////////////////////////////////////////////
////////////////
    n_boundaries = 0;
    profile = getProfile();
```

```
    for (i = 1; i < profile.length; i++)
    {
        Difference = profile[i] - profile[i-1];
        if (profile[i] == 255 && Difference > 0)
        {
            n_boundaries = n_boundaries + 1;
        }
    }

    ////////////////////////////////////////////////////////////////
    // Write the number of boundaries, line length and average spacing
    ////////////////////////////////////////////////////////////////
    setResult("Number of boundaries", j, n_boundaries);
    setResult("Line length", j, profile.length);
    setResult("Average spacing", j, profile.length / n_boundaries);
}


////////////////////////////////////////////////
// Caclulate the Dentritic Arm Spacing (DAS)
////////////////////////////////////////////////
DAS_sum = 0;
Number_of_lines = 0;


for (k = 0; k < nResults; k++)
{

    DAS = getResult("Average spacing", k);
    Test_boundary = getResult("Number of boundaries", k);
    if (Test_boundary > 0)
    {
        DAS_sum = DAS_sum + DAS;
        Number_of_lines = Number_of_lines + 1;
    }

}

//Average_DAS = DAS_sum / nResults;
Average_DAS = DAS_sum / Number_of_lines;
setResult("Average DAS", 0, Average_DAS);
```